Post-glacial evolution of alpine environments in the western Mediterranean region: The Laguna Seca record

Alejandro López-Avilés [a,*], Gonzalo Jiménez-Moreno [a], Antonio García-Alix [a,b], Fernando García-García [a], Jon Camuera [c], R. Scott Anderson [d], Jorge Sanjurjo-Sánchez [e], Carlos Arce Chamorro [e], José S. Carrión [f]

[a] Departamento de Estratigrafía y Paleontología, Universidad de Granada, Avenida Fuente Nueva s/n, 18071 Granada, Spain
[b] Instituto Andaluz de Ciencias de la Tierra (IACT), CSIC-UGR, Avenida de las Palmeras 4, 18100 Armilla, Granada, Spain
[c] Department of Geosciences and Geography, University of Helsinki, Helsinki 00014, Finland
[d] School of Earth and Sustainability, Northern Arizona University, Flagstaff, AZ 86011, USA
[e] University Institute of Geology Isidro Parga Pondal, University of A Coruña, Campus de Elviña s/n, 15011 A Coruña, Spain
[f] Department of Plant Biology, Faculty of Biology, University of Murcia, Campus Universitario 5, 301000 Murcia, Spain

A R T I C L E   I N F O

A B S T R A C T

In an effort to understand how alpine environments from the western Mediterranean region responded to climate variations since the last glacial-interglacial transition, a detailed chronological control and sedimentological analysis, supported by magnetic susceptibility, total organic carbon and C/N data, were carried out on the sedimentary record of Laguna Seca (LS). This is a latitudinal and altitudinally (2259 masl) key alpine wetland site located in the easternmost area of the Sierra Nevada, southern Iberian Peninsula, where sediments accumulated during Heinrich Stadial 1, Bølling-Allerød (B-A) and the Younger Dryas (YD) - previously unrecorded in alpine Sierra Nevada. Climate controlled sedimentation in LS and three coarse-grained and one fine-grained facies association are differentiated, which help us decipher the paleoenvironmental evolution of LS: (1) subaerial cohesionless debris flows during a paraglacial stage; (2) till or nival diamicton during a small glacier/nivation hollow stage; (3) massive mudstone by suspension settling of clays into standing water during a lacustrine stage; and (4) frost-shattering breccia deposited inside the lacustrine stage, probably during the YD, and linked to a periglacial substage. The development of a previously existing small glacial cirque during the Last Glacial Maximum (LGM) in the LS basin at an elevation between 2500 and 2300 m could be supported by the important availability of slope sediments glacially-conditioned such as debris flows, reworked by paraglacial slope processes during the first deglaciation stages, confirming previous studies of landforms in the catchment area and the LGM-Equilibrium Line Altitude estimation above 2400 masl in Sierra Nevada. Mean sediment accumulation rates in the LS sedimentary units (4.21 and 0.28 mm/yr during the paraglacial - small glacier/nivation stage and the lacustrine stage, respectively) confirm that geomorphic activity accelerated just after glaciers retreated due to a slope adjustment and high availability of glacially conditioned sediments. An abrupt change in paleoenvironmental and paleoclimatic conditions occurred in LS at ~ 15.7 cal kyr BP. This change was probably due to an increase in temperature and precipitation in the western Mediterranean region during the B-A. At LS, this resulted in significant ice-melt, forming a deep-water lake in LS with important organic matter contribution until the end of the Early Holocene (except in the YD when the lake level probably dropped), but elsewhere a general glacier recession in the Sierra Nevada and an expansion of the Mediterranean forest in the southern Iberian Peninsula. Finally, the general long-term aridification that occurred during the Middle Holocene until the present in the western Mediterranean region triggered an important environmental change transforming LS into an ephemeral wetland with an increase in aquatic productivity.

1. Introduction

Sharp environmental changes, called Terminations, mark the end of the glacial episodes and the transition toward interglacial conditions as revealed by oxygen isotope profiles both from ocean and terrestrial records (Cheng et al., 2009). Those abrupt ends of glacial episodes are generally lacking or poorly recorded and/or preserved in continental records from mid-latitudes (i.e., Mediterranean region) due to reduced sedimentation rate (i.e., speleothem growth, McDermott, 2004), incision of alluvial sediments or low lake levels (PMIP Global Lake Status Database).

Glacial sedimentology has played a secondary role in the reconstruction of Quaternary glacial environments (in contrast to glacial geomorphology, Bennett and Glasser, 2009; Benn and Evans, 2010) due to the difficulty in identifying glacially-derived diamicton from other origins in strongly seasonal climates (McCaroll et al., 2001; Benn and Evans, 2010; Hambrey and Glasser, 2012). Sedimentary features, such as fabric, texture, grain-size and sorting, and other, represent lithologic evidence that helps reconstruct palaeoenvironments when the relationship between climate and sediments is well understood. However, sedimentary records in alpine glacial environments are difficult to interpret as fluvial, lacustrine and mass-flow processes operate before, during and after the dominantly-glacial environmental stage. Refinement of the sedimentary facies models in alpine settings is needed to recognize, from within cores, the high variability of sediments corresponding to different environments (glacial, paraglacial and/or periglacial) that occurred during the glacial terminations in glaciated mountains.

In many low-elevation and/or low-latitude mountain ranges where large-scale glaciation is lacking or marginal, isolated glaciers occurred in relict cirques within favorable topographic settings (Sanders et al., 2013). As cirque glaciers or nivation hollows are the first and the last forms to exist during a glacial cycle, these have been used as highly sensitive paleoclimate indicators (i.e., to reconstruct paleo-Equilibrium Line Altitude (ELA)) (Barr and Spagnolo, 2015; Knazková et al., 2021). Incised cirque-like forms represent high-altitude areas where paraglacial sediment is partly trapped. Therefore, the sedimentary successions in those glacial or nival small mountain sinks provide a relatively more continuous record than other glacial settings such as glacier valleys, which represent sediment transferring systems but not preferential accumulation settings, as revealed by non-continuous cosmogenic chronology of glacial-periglacial valley landforms (Gómez-Ortiz et al., 2012). Small glaciers, long-lived snow-patches in relict glacier cirques or nivation hollows have been shown to be highly sensitive to past short-term climate change (Brown et al., 2010).

Although there are evidences of Laurentide and Scandinavian ice recession at ~ 20 cal kyr BP, deglaciation in the northern Hemisphere commenced at ~ 19 cal kyr BP (Clark et al., 2009; Denton et al., 2010). In the Mediterranean fringe, glacier recession also started after the Last Glacial Maximum (LGM), and intensified after ~ 15 cal kyr BP (Palacios et al., 2016; Rolland et al., 2020). Between these dates some Mediterranean mountain ranges registered a glacier re-advance, as is the case of the Sierra Nevada; however, these glaciers massively melted at ~ 15 cal kyr BP (Palacios et al., 2016), allowing the development of alpine wetlands (Castillo Martín, 2009). Glaciers only reappeared in this area during the coldest periods such as Heinrich Stadial 1 (HS1) and the Younger Dryas (YD) (García-Ruiz et al., 2016; Hughes and Woodward, 2017; Palacios et al., 2017; Ribolini et al., 2018; Palma et al., 2017; Oliva et al., 2014; Palacios et al., 2016). The Sierra Nevada wetlands are highly sensitive areas to climate change and their sediments accurately record its footprint, preserving a high-quality signal of past natural environments (García-Alix et al., 2017, 2018). However, previous studies on sedimentary records from the alpine Sierra Nevada showed that wetland formation in glacier cirque areas occurred in the YD-Early Holocene transition and a record of sedimentation older than that was yet to be found (Anderson et al., 2011; Jiménez-Moreno and Anderson,

2012; García-Alix et al., 2012, 2017, 2018; Jiménez-Espejo et al., 2014; Jiménez-Moreno et al., 2013, 2020; Ramos-Román et al., 2016; Mesa-Fernández et al., 2018; Manzano et al., 2019; Toney et al., 2020; López-Avilés et al., 2021). This is probably due to glacial erosion, which occurred during the YD at the high elevation glacial cirque areas (Anderson et al., 2011; Palacios et al., 2020). Longer and older sedimentary sequences than the Holocene potentially occur in sedimentary basins in Sierra Nevada at lower elevations, below the erosive action of alpine glaciers. Searching for a record longer than the Holocene in Sierra Nevada, which would register environmental changes during the last deglaciation, has been a goal of our research team for some time.

In this study we analyzed the longest and oldest sedimentary record retrieved, until now, in the alpine Sierra Nevada. The Laguna Seca (LS) record covers the last ~ 18 cal kyr BP and is located in the easternmost area of the Sierra Nevada. Here we focus on the chronological control and sedimentological analysis supported by magnetic susceptibility (MS), total organic carbon (TOC) and carbon/nitrogen (C/N) data with the main goal of understanding how alpine environments in Sierra Nevada and the western Mediterranean region responded to climate variations from the last glacial-interglacial transition.

2. Background

2.1. Sierra Nevada

Sierra Nevada is the highest mountain range in southwestern Europe. It is characterized by an east–west orientation, ~80 km long, a width between 15 and 40 km, and includes the Mulhacén and Veleta peaks, which are the highest peaks of the Iberian Peninsula with 3478 and 3398 masl, respectively (Fig. 1a, b). The present geomorphological landscape of Sierra Nevada is consequence of oscillations in the climate conditions that shaped the highest sectors of this massif through glacial and periglacial morphodynamics during the Quaternary (Oliva et al., 2014, 2016). Glacial erosion during the cold stages of the Last Glaciation and YD generated numerous cirque depressions above 2600 masl where small lakes and waterlogged areas with abundant vegetation (peatlands, locally known as borreguiles) subsequently developed (Castillo Martín, 2009).

2.2. Climate

Climate in the study area is Mediterranean with mild winters and hot and dry summers (Agencia Estatal de Meteorología, 2021). Several parameters such as precipitation, temperature and wind speed-direction were monitored between 2008 and 2016 at a weather station ~ 3.5 km from Laguna Seca. Mean annual precipitation is around 581 mm/yr. The driest month is July with 2 mm and the most humid month is March with 114 mm of rainfall. Mean annual temperature is 6.3 ± 0.5 °C. February is the coldest month (-1.2 ± 1.7 °C) and July the warmest one (16.8 ± 1.2 °C). Mean annual speed and direction of the winds are 6.5 m/s and 245°, respectively (Organismo Autónomo Parques Nacionales, 2021).

2.3. Laguna Seca wetland

LS (37°05′53′′N, 2°58′05′′W) is a small endorheic alpine depression situated at 2259 masl in the eastern side of the Sierra Nevada (Fig. 1b, c, d). At present, LS is covered with ice and snow in winter. According to the wind pattern, the LS basin lies to leeward, preventing snow deflation and favoring its accumulation by redepositing it from the windward faces (southwest face of the Chullo peak). During spring and early summer, the water table is shallow and can reach a maximum level of ~ 0.5 m, but LS dries up in late summer (Fig. 1e). The catchment area covers ~ 58.8 ha and ranges in elevation from 2259 to 2540 masl (Fig. 1c). The basin catchment area is characterized by low-degree metamorphic mica schists of the Nevado Filábride complex (Martín
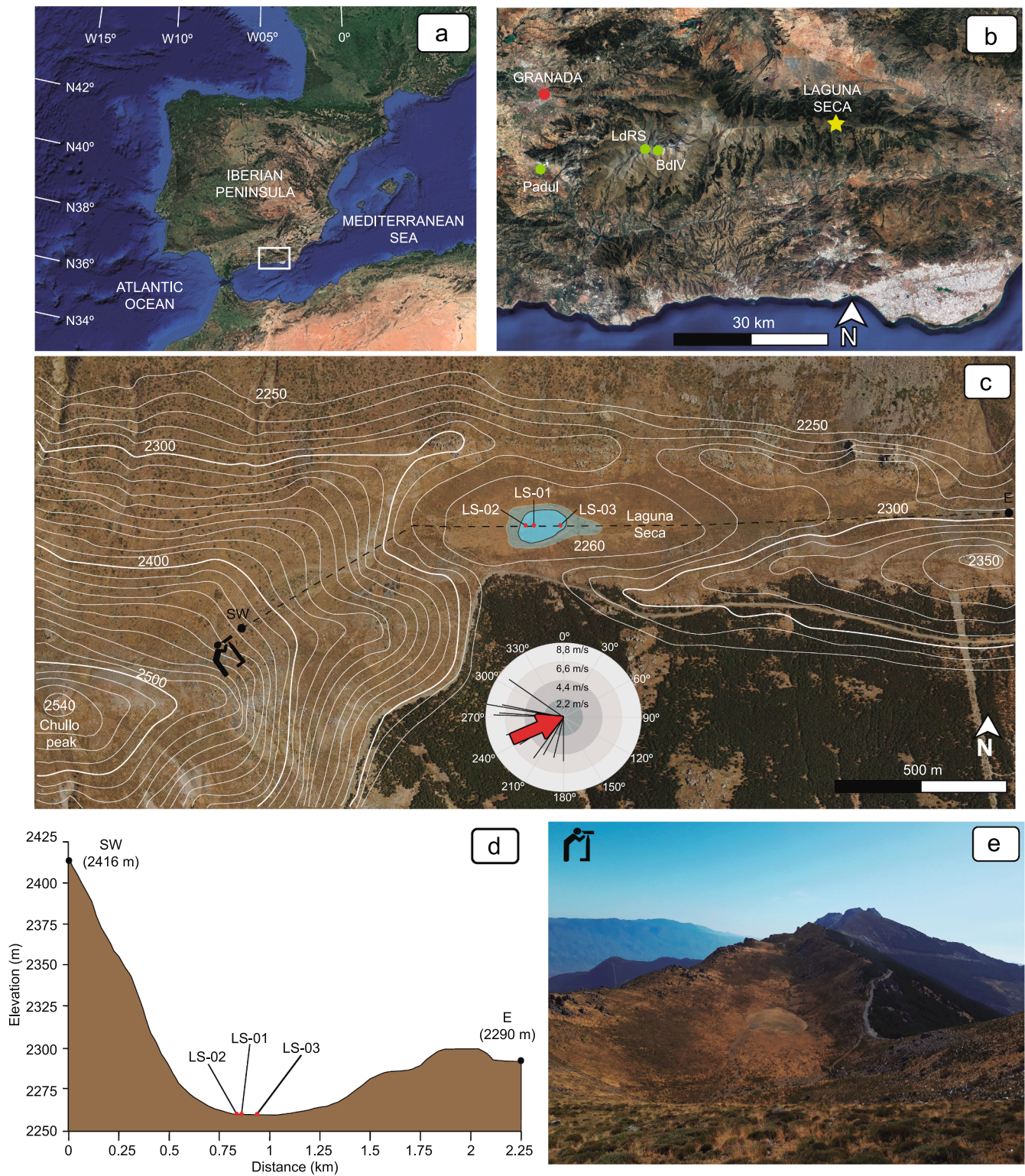
Fig. 1. (a) Location of the Sierra Nevada, southeastern Iberian Peninsula, western Mediterranean region (b) Laguna Seca (this study) location within Sierra Nevada, BdlV (Borreguiles de la Virgen; Jiménez-Moreno and Anderson, 2012), LdRS (Laguna de Río Seco; Anderson et al., 2011) and the Padul wetland (Camuera et al., 2018) (c) LS catchment area with the three sedimentary records obtained (red points). Also, wind rose showing mean monthly distributed wind direction and wind speed values. Red arrow indicates the predominant wind direction (d) Topographical profile, to scale, in a southwest-east (SW-E) direction (e) SW-E panoramic view of LS, September of 2019 (Lagunas de Sierra Nevada, 2021). Picture sources: a, b and c) Google Earth; e) Raquel Monterrubio Sanz. (For interpretation of the references to color in this figure legend, the reader is referred to the web version of this article.)

Martín et al., 2010). According to Simón et al. (2000), the main land-forms in LS basin are 1) a glacial cirque situated at 2370 masl in the western slope, originated by undated cold episodes, and 2) a gelifluction flow and gelifraction lobes located in the western and southeastern slopes, respectively, originated by a relatively recent cold episode (Fig. 2). The soil development is scarce with tundra-type crior-omediterranean vegetation (Valle, 2003). This alpine lake is at present-day located right above treeline, with oromediterranean vegetation, mostly characterized by *Pinus sylvestris, P. nigra, Juniperus* spp. and with shrubs of the Fabaceae, Cistaceae and Brassicaceae families, among others, growing at lower elevations.

3. Material and methods

3.1. LS site core drilling

Three sediment cores, LS-01, LS-02 and LS-03, with lengths of 14.1, 9.6 and 8.1 m, respectively, were recovered in September 2014 from the depocentre area of LS (Fig. 1c, d and 2). LS-01 and LS-02 were taken with an approximate distance of 5 m, with LS-02 in a slightly more proximal (west) position to reconstruct the lateral variation in the sediment architecture. LS-03 was taken 50 m further to the east, in a more distal position, to assess the lateral consistency of the stratigraphic succession. Cores were collected with a Rolatec RL-48-L drilling machine equipped with a percussion corer from the Scientific Instrumentation Center of the University of Granada (CIC-UGR). Sedimentary cores were transported to the University of Granada and stored in a refrigerated room at 4 °C.

3.2. Chronology

The chronology of the LS sedimentary record is based on nine Accelerator Mass Spectometry (AMS) radiocarbon and four optically stimulated luminescence (OSL) dates from the LS-01 sediment core. Radiocarbon dates were obtained from bulk sediment samples in the uppermost 4.38 m of the core. All the bulk samples (except Poz-72964, Poz-72965, Poz-72966 and Poz-72967) were pre-treated with hydrochloric acid (HCl) and hydrofluoric acid (HF) to remove carbonates and silicates, thus concentrating the organic matter. Radiocarbon dates were converted into calendar years before present (cal yr BP) using the IntCal20.14c curve (Reimer et al., 2020) by means of Calib 8.2html software (Stuiver et al., 2021). OSL dates were obtained in the last 9.27

m of the core (Table 1). A Bayesian age-depth model for LS-01 was developed using ^{14}C and OSL data and the R modeling package "R-Bacon (v. 2.5.1 - February 2021)" (Blaauw and Christen, 2011). The best age model was obtained using 182 sections with 7.75 cm. A prior accumulation rate as a gamma distribution with shape 2.1 and mean 35 (yr/cm) were set for the uppermost 4.48 m of the core. Sedimentation rates abruptly changed at 4.48 m and the prior mean accumulation rate was set to 2.4 (yr/cm) from that point to the bottom of the core. A model memory as a beta distribution with strength 50 and mean 0.3 were set for the accumulation variability (Fig. 3).

3.2.1. OSL sample preparation

Samples for OSL dating were opened under subdued red light in the luminescence laboratory of the University of A Coruña. Coarse grains (90–180 μm diameter) were sieved, dried and treated with HCl and hydrogen peroxide (H_2O_2) to remove carbonates and organic matter, respectively. Feldspar and heavy minerals were removed by density separation, using sodium polytungstate solutions of 2.58 g cm^{-3} and 2.68 g cm^{-3} specific gravity. The obtained quartz grains (between 2.58 g cm^{-3} and 2.68 g cm^{-3}) were etched in HF to remove any remaining feldspars and to etch the surface of quartz grains. Later, a final HCl washing was applied to remove any remaining soluble fluorides. The obtained quartz grains were checked with infrared (IR) stimulation to ensure that feldspars were absent. Quartz grains were mounted on small multi-grain aliquots of 20 ± 2 grains (1 mm diameter).

3.2.2. OSL measurements and dose rates estimation

An automated Risø DA-15 TL/OSL reader system was used for measurements. The reader is equipped with blue (470 ± 30 nm) light-emitting diodes (LEDs) and a 9235QA photomultiplier tube (PMT) to record signals. An optical 6 mm-thick Hoya U-340 filter was placed between the aliquots and the PMT to measure the 340 ± 80 nm emission (UV). Laboratory doses were given using a ^{90}Sr/^{90}Y beta source mounted on the reader emitting a 0.100 ± 0.003 Gy s^{-1} dose. The blue-OSL (BL-OSL) single-aliquot regenerative dose (SAR) protocol (Murray and Wintle, 2000, 2003) was used to estimate the equivalent doses (D_es). The multi-grain aliquots were stimulated for 40 s at 125 °C, using the first 0.4 s to measure OSL and the last 4 s for background subtraction. Preheat tests were previously performed for all samples being a preheat temperature of 200 °C chosen. Dose recovery tests were also performed on bleached aliquots (200 s BL-OSL bleaching twice at room temperature separated by a pause of 10,000 s) after irradiation with beta doses
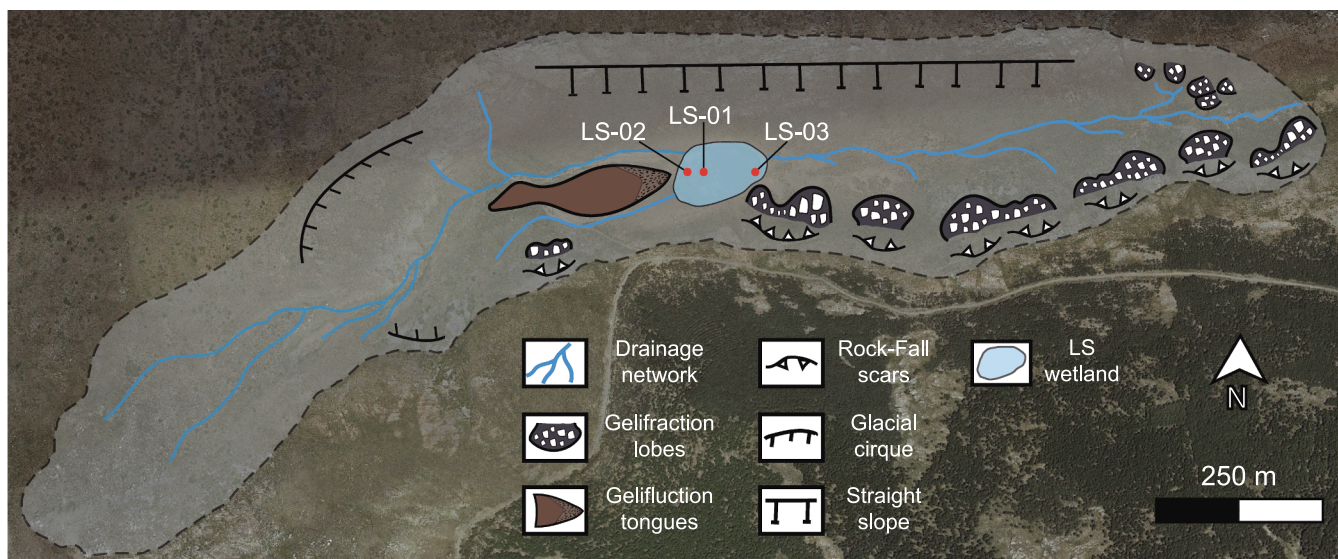

Fig. 2. Geomorphologic features of the LS catchment area (Modified from Simón et al., 2000) with the three sedimentary records obtained (red points). (For interpretation of the references to color in this figure legend, the reader is referred to the web version of this article.)

Table 1

Age data for LS-01. Radiometric ages were calibrated using IntCal20.14c curve (Reimer et al., 2020) with Calib 8.2 (http://calib.org/calib/). OSL dates are marked with asterisk. In italic font, radiocarbon dates rejected. Acronyms: TBS; pre-treated bulk sediment with HCl and HF, BS; bulk sediment.

Laboratory code	Material	Depth (m)	Dating method	Age ^{14}C yr BP ± 1σ OSL*	Calibrated age (cal yr BP) 2σ range
Reference Age		0	Present		−65
Beta-544146	*TBS*	*0.37*	^{14}*C*	*11070 ± 30*	*12910–13088*
Beta-452041	TBS	0.60	^{14}C	1690 ± 30	1528–1695
Beta-544147	*TBS*	*0.83*	^{14}*C*	*15960 ± 40*	*19129–19425*
Beta-452042	TBS	1.20	^{14}C	3880 ± 30	4160–4414
Beta-452043	TBS	1.80	^{14}C	5050 ± 30	5720–5903
Beta-458581	TBS	2.26	^{14}C	6620 ± 40	7431–7570
Beta-458581	TBS	2.72	^{14}C	7200 ± 30	7939–8158
Beta-458583	TBS	2.94	^{14}C	7380 ± 30	8037–8324
Poz-72963	Algae	3.00	^{14}C	8920 ± 50	9821–10219
Poz-72964	*BS*	*3.00*	^{14}*C*	*11580 ± 60*	*13317–13580*
Beta-458584	TBS	3.21	^{14}C	9370 ± 30	10505–10686
Poz-72965	*BS*	*3.60*	^{14}*C*	*30900 ± 400*	*34541–36090*
Beta-544148	*TBS*	*3.81*	^{14}*C*	*23860 ± 100*	*27748–28288*
Beta-544149	TBS	4.38	^{14}C	13050 ± 40	15474–15795
OSL-LS-Dr.09		4.83–5.02	OSL	11400 ± 800*	
Poz-72966	*BS*	*5.40*	^{14}*C*	*37200 ± 800*	*40679–42578*
OSL-LS-Dr.14		8.03–8.17	OSL	13400 ± 1300*	
Poz-72967	*BS*	*9.00*	^{14}*C*	*33800 ± 600*	*36956–40089*
OSL-LS-Dr.21		12.29–12.39	OSL	12600 ± 1000*	
OSL-LS-Dr.24		13.89–14.01	OSL	13600 ± 1400*	

similar to the assessed $D_e s$ (Murray and Wintle, 2003). The dose-rates ($D_r s$) were assessed after estimating ^{40}K and ^{238}U, ^{235}U and ^{232}Th decay chain activities using Low Background Gamma Spectrometry on bulk samples (Table 2). Samples were samples in sealed flask during 30 days for Rn equilibration and later measured in a coaxial Camberra XTRA gamma detector (Ge Intrinsic) model GR6022 within a 10 cm-thick lead shield. Conversion factors of Guerin et al. (2011) were used to assess the $D_r s$. The alpha contribution was neglected and the beta dose-rate corrected (Brennan et al., 2003) due to HF etching of quartz grains. The water content and saturation of samples were assessed in the laboratory and the average water content was assessed considering that samples were saturated most of the burial time. The cosmic dose rates were calculated according to Prescott and Hutton (1994) (Table 2).

3.3. Lithology

The three sediment cores were split longitudinally and described

thoroughly in the laboratory with respect to sedimentary facies characteristics. Facies and facies associations were distinguished according to standard sedimentary features (colour, texture-grain size, clast-roundness and clast-sphericity, clast fabric, long axis dipping) (Fig. 4). The grain size was obtained from the average size of ten randomly selected grains and the roundness according to Powers (1953). The facies classification and codes are modified from Miall (1978). The spatial distribution of the cores in LS allowed the development of a two-dimensional schematic model showing the lateral changes in lithofacies and thickness of the different stratigraphic units (Fig. 5).

3.4. Magnetic susceptibility

MS was measured for all of cores with a Bartington MS2E meter in international system of units (SI × 10^{-4}) every 0.5 cm (Fig. 5). The measuring time period was 10 s. MS is commonly used in lacustrine deposits and has also been used in the differentiation and stratigraphic correlation of sedimentary facies in glacial tills (Vonder-Haar and Hilton-Johnson, 1973). A synthetic MS reconstruction for the LS sedimentary record was also generated by averaging the MS Z-scores (x-mean/σ) of the three cores (LS-01, LS-02 and LS-03) at 0.5 cm increments in order to characterize and synthesize the different facies and units, and thus to facilitate the comparison of this variable with other local and regional proxies (Fig. 5).

3.5. Organic geochemistry

A total of 198 samples were taken from the LS-01 core for CHNS analyses with a sampling interval of ∼ 5 cm. One cubic centimeter of each sample was decalcified overnight with HCl 1 N, and rinsed several times with MilliQ water until a neutral pH. About 5 mg of the decalcified sample was encapsulated in tin capsules and analysed by means of a CHNS Elemental Analyzer Thermo Scientific Flash 2000 at the CIC-UGR. Helium was used as gas carrier and the flash combustion was produced at 1000 °C. The equipment was calibrated every day using a certified sulfanilamide standard and the precision of the measurements was better than ± 0.1 %. Atomic C/N ratio was calculated from the division of total carbon and nitrogen yielded by the elemental analyzer by their respective atomic weights. % TOC was calculated from the percentage of carbon recalculated by the weight of the sample before and after decalcification (Fig. 5).

4. Results

4.1. Chronology

4.1.1. AMS radiocarbon dating

Sixteen radiocarbon dates from organic matter were obtained to build the age-depth model of LS-01 core. To assess the reliability and accuracy of the dates, two criteria have been considered: the stratigraphic location and the origin of organic matter.

The stratigraphic criterion is based on the coherence between ages and depths in the cores. Among the sixteen radiocarbon dates analyzed in stratigraphic order, seven showed seemingly excessive old ages, which could be due to redeposition of old organic matter. Four of these anomalous samples (Poz-samples) were not treated by means of HCl and HF to remove carbonate and siliciclastic material, and thus, the concentration of organic matter was lower than in the other samples. The disagreement between two samples taken at the same depth, 300 cm, Poz-72963 (pre-treated and rich in algae) and Poz-72964 (bulk sediment without pre-treatment) would suggest that bulk sediment samples without previous treatment exhibited no reliable ^{14}C ages (Table 1). The other three samples that show anomalous ages (Beta-544146, Beta-544147 and Beta-544148) were pre-treated with HCl and HF but were discarded for showing stratigraphically incoherent ^{14}C ages. The nine remaining samples showed stratigraphically coherent ^{14}C ages.
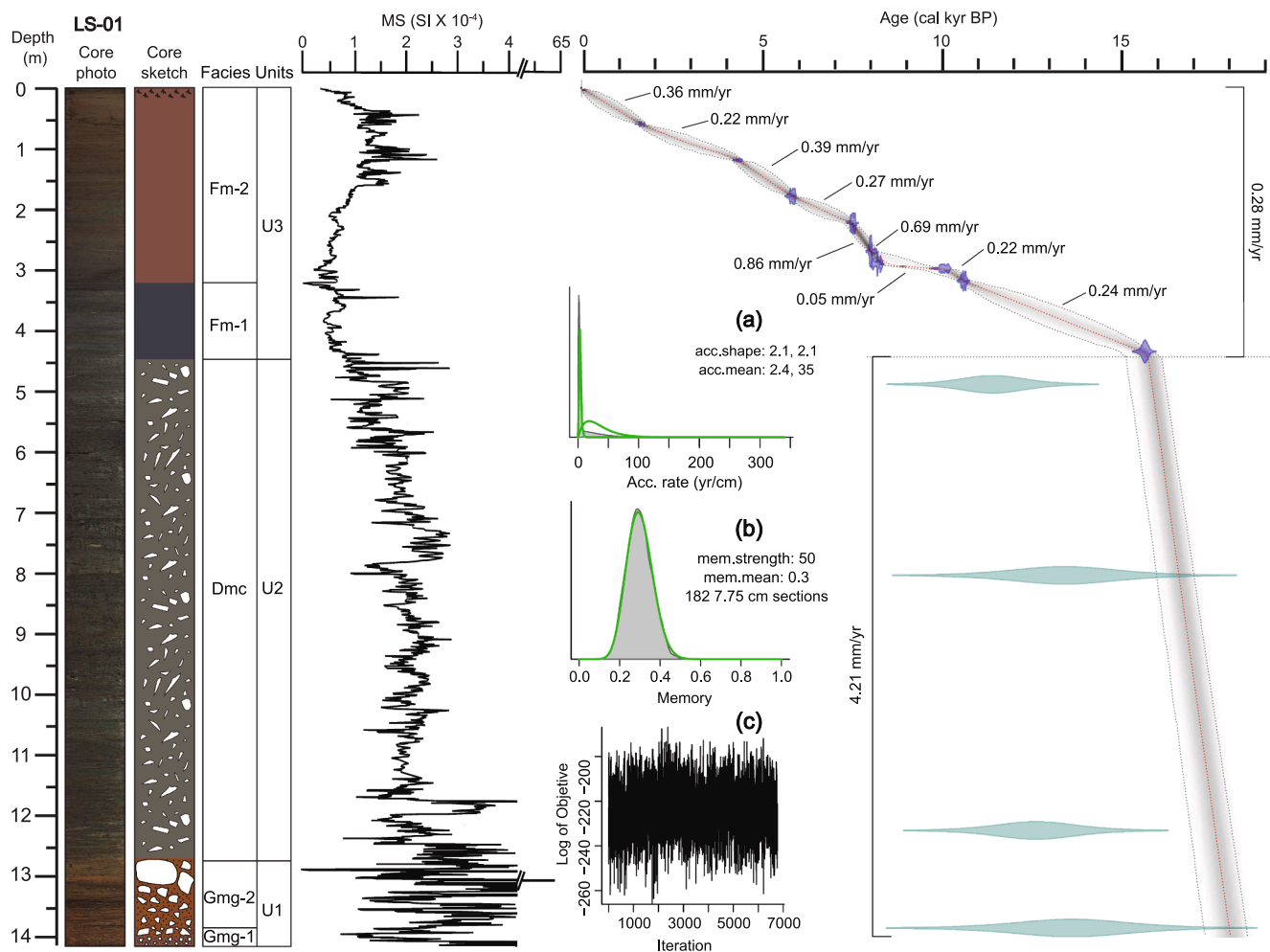
Fig. 3. Profile of LS-01 sedimentary record. From left to right: core photography, core lithofacies sketch, sedimentary facies (see text for facies description), stratigraphic units (U1-U3), magnetic susceptibility (SI units) and bayesian age-depth model including the sediment accumulation rates (mm/yr). In the age model, dark blue shaded areas represent calibrated ^{14}C dates and their uncertainties. Outer dotted lines indicate 95% confidence intervals being the central dotted red line the weighted median age. Horizontal dotted line indicates the break in the sedimentation rate. Light blue shaded areas represent OSL dates and their uncertainties. Parameters of age model: (a) prior and posterior distribution of the accumulation rate (green and grey lines respectively) (b) prior and posterior distribution of the model memory (green and grey lines respectively) and (c) log distribution of the Markov Chain Monte Carlo (MCMC) model iterations. (For interpretation of the references to color in this figure legend, the reader is referred to the web version of this article.)

Table 2.

Parameters for dose-rate assessment: water content (%W), activity concentration of radionuclides ([40]K, [232]Th, [238]U and [226]Ra) and estimated beta ($D_{r\beta}$), gamma ($D_{r\gamma}$) and cosmic (D_{rc}) dose-rates. The activity concentration of radionuclides is expressed in becquerel/kilogram (Bq/kg). The estimated beta, gamma and cosmic dose-rates are expressed in gray/kiloyear (Gy/kyr).

Sample	W (%)	[40]K (Bq/kg)	[232]Th (Bq/kg)	[238]U (Bq/kg)	[226]Ra (Bq/kg)	$D_{r\beta}$ (Gy/kyr)	$D_{r\gamma}$ (Gy/kyr)	D_{rc} (Gy/kyr)
OSL-LS-Dr.09	30 ± 3	769 ± 27	74.3 ± 1.5	48.3 ± 2.5	40.8 ± 9.1	1.71 ± 0.09	1.24 ± 0.07	0.17 ± 0.02
OSL-LS-Dr.14	30 ± 5	687 ± 23	55.7 ± 2.7	37.8 ± 8.2	38.5 ± 10.7	1.55 ± 0.11	1.13 ± 0.09	0.12 ± 0.01
OSL-LS-Dr.21	35 ± 5	851 ± 30	43.2 ± 5.5	32.7 ± 7.8	38.5 ± 10.7	1.68 ± 0.12	1.06 ± 0.10	0.08 ± 0.01
OSL-LS-Dr.24	33 ± 3	573 ± 22	53.8 ± 1.2	30.3 ± 7.0	39.3 ± 4.7	1.30 ± 0.06	0.97 ± 0.05	0.07 ± 0.01

Furthermore, radiocarbon dating of organic matter can provide biased and overestimated ages in lake sediments, depending on its origin (Meyers, 1994) and the nature of the catchment rocks (Philippsen, 2013). If the organic matter is autochthonous (algae or lacustrine/catchment plants), the obtained date is usually reliable, as such matter was produced in situ simultaneously with the sedimentation process (Meyers, 1994). However, when the organic matter is allochthonous (i. e., it comes from soil erosion) it does not necessarily have to be coeval with the sedimentation process, so it can provide older ages. We believe that this is the case with the radiocarbon dates that showed too old ages.

Another variable that has to be considered in freshwater systems is the potential reservoir effect on autochthonous organic matter (e.g., Philippsen, 2013). In lacustrine sediments this is usually related to the presence of older carbonate rocks in the catchment basin that could contribute to the dissolved organic carbon (DIC) pool of lake waters, modifying the ^{14}C signal of freshwater organism (Philippsen, 2013). Since the catchment basin of Laguna Seca consists of low-degree metamorphic mica schists, the potential reservoir effect on the autochthonous organic matter of the lake is negligible.

The radiocarbon dates provided ages starting at ∼ 15.6 cal kyr BP for

Fig. 4. Compilation of the facies association, facies and their sedimentary features presented in the three sedimentary records (LS-01, LS-02 and LS-03) from LS. Facies MS values are from average of facies in LS-01, LS-02 and LS-03. TOC and C/N values are only for LS-01. From left to right: facies association, core photography/texture sketch, facies, sketch, sedimentary features and facies interpretation. In the sketch section, the letters M, D and G mean mud, diamicton and gravel. Red triangles represent inverse grading. (For interpretation of the references to color in this figure legend, the reader is referred to the web version of this article.)

the uppermost 4.38 m of the LS-01 sedimentary record (Table 1; Fig. 3).

4.1.2. Dose-rate estimates and OSL ages

The gamma spectrometry of the samples showed ^{235}U activity concentrations below detection limits, and variable activity concentrations for ^{40}K, and ^{238}U and ^{232}Th decay chains (Table 2). No disequilibrium was observed in the ^{238}U and ^{232}Th decay chains. The estimated water content was near saturation for all samples. The obtained D_rs range from 2.34 ± 0.08 Gy kyr^{-1} to 3.13 ± 0.12 Gy kyr^{-1} (Table 3). A 200 °C preheat was chosen for the BL-OSL SAR after preheat tests. Quartz grains

showed dim signals, providing the D_es of individual aliquots with high standard deviations and poor recycling ratios, being rejected between 40 % and 60 % of the measured aliquots. The resulting D_e distributions provided non-skewed dispersions with low kurtosis. The Central Age Model (CAM; Galbraith et al., 1999) was used to assess the D_es. The overdispersion of the CAM provided values from 21.6 ± 6.2 % to 45.8 ± 8.0 % (Table 3). This high overdispersion seems to be caused by the internal quartz sensitivity, as observed from the recorded dim signals. Indeed, the dose recovery tests provided ratios between 0.9 and 1.1 but high overdispersion values, between 14.3 ± 7.6 % and 24.9 ± 9.9
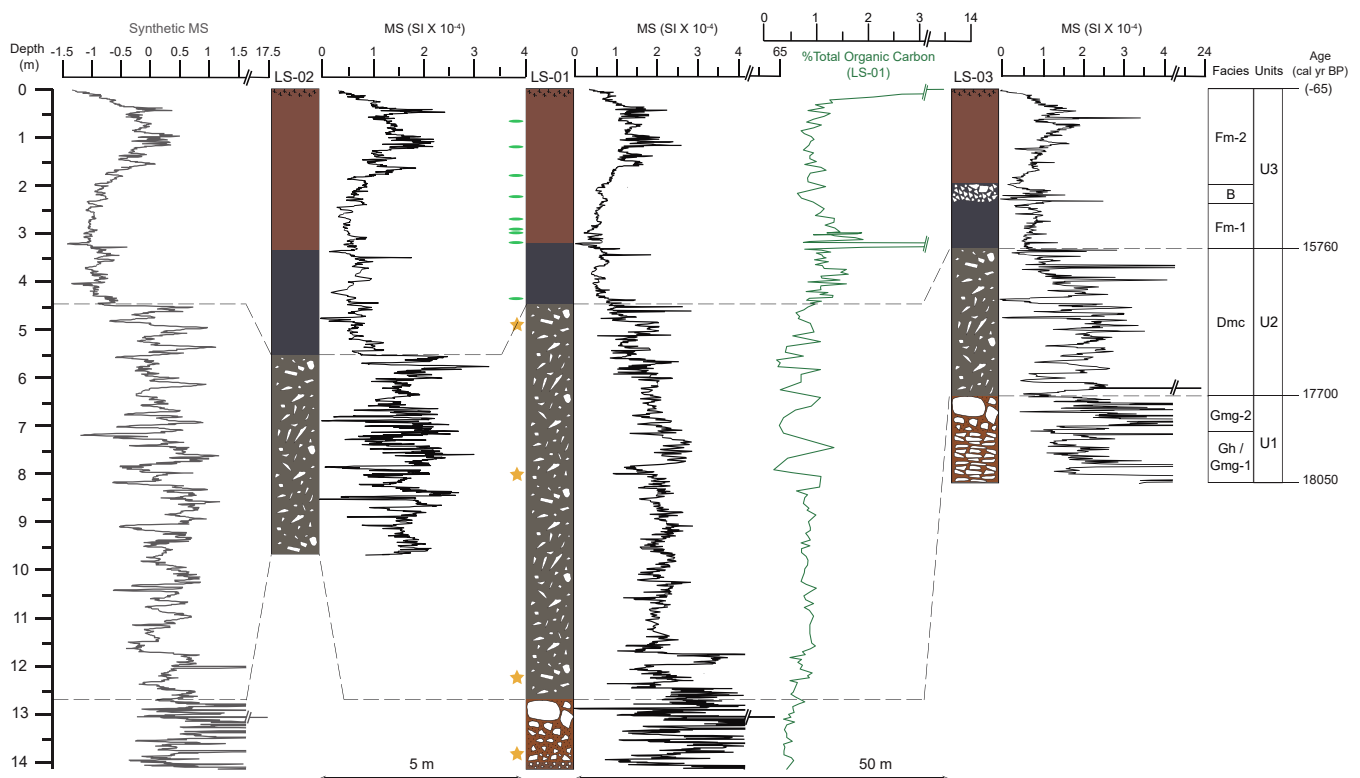
Fig. 5. Chronostratigraphic correlation of the three sedimentary records (LS-01, LS-02 and LS-03) obtained in LS. The MS (three cores), %TOC (only LS-01) and the synthetic MS reconstruction from the mean Z-scores are represented. Three stratigraphic units (in age) and seven facies are also represented. Radiocarbon and OSL ages are expressed in green lines and yellow stars, respectively, in core LS-01. The distances between sedimentary records are no to scale. (For interpretation of the references to color in this figure legend, the reader is referred to the web version of this article.)

Table 3

Data obtained and resulting OSL ages: total dose-rate (D_r), N measured aliquots (accepted/measured) and overdispersion (% Over). The total dose-rate and the ages are expressed in gray/kiloyear (Gy/kyr) and kiloyear (kyr).

Sample	D_r (Gy/kyr)	N	D_e (Gy)	Over (%)	Skewness	Kurtosis	Dose recovery Ratio	Dose recovery Over (%)	Age (kyr)
OSL-LS-Dr.09	3.13 ± 0.12	29/48	35.7 ± 2.2	21.6 ± 6.2	0.20	2.55	0.94 ± 0.07	17.5 ± 7.8	11.4 ± 0.8
OSL-LS-Dr.14	2.80 ± 0.14	32/62	37.4 ± 3.2	41.5 ± 7.1	−0.35	2.80	0.90 ± 0.06	14.3 ± 7.6	13.4 ± 1.3
OSL-LS-Dr.21	2.83 ± 0.15	29/70	33.7 ± 2.8	31.5 ± 7.5	0.38	1.79	0.98 ± 0.08	24.9 ± 9.9	12.6 ± 1.0
OSL-LS-Dr.24	2.34 ± 0.08	29/54	31.9 ± 3.2	45.8 ± 8.0	0.02	1.56	0.91 ± 0.07	21.5 ± 7.3	13.6 ± 1.4

(Table 3). Such values are unusual in recovery dose experiments (Galbraith and Roberts, 2012) and support the hypothesis of the poor internal quartz sensitivity as the cause of the high overdispersion. In addition, we cannot discard beta microdosimetry as a possible cause of such overdispersion, since the OSL samples correspond to heterogeneous sedimentary facies (Figs. 3 and 5). Such heterogeneity can also have effects on the estimated gamma dose rate (Nathan et al., 2003) causing slight deviations in the resulting ages of some of the samples. No evidence of partial bleaching is observed either in OSL signals, aliquot D_e distributions or stratigraphical incoherence of ages. Thus, the CAM seems to provide reliable ages, that are between 11.4 ± 0.8 kyr to 13.6 ± 1.4 kyr (Table 3).

4.1.3. Bayesian age-depth model and sediment accumulation rates (SARs)

The best combination of AMS radiocarbon and OSL dating were used to build a bayesian age-depth model for the LS sedimentary record (Fig. 3). OSL dating was used between 4.48 m and the bottom of the LS-01 core since there was not enough organic matter for AMS radiocarbon dating. The facies dated with OSL correspond to heterogeneous deposits (see section 4.2; Figs. 3 and 5). Heterogeneity in the sediment generates, on the one hand, variations in sediment beta-microdosimetry (Mayya

et al., 2006), which affects the dispersion of OSL ages. On the other hand, it affects the estimation of the gamma dose rate (Nathan et al., 2003), since the radiation rate is obtained from a portion of the sediment in the core and cannot be measured in situ. The gamma dose rate affecting the quartz comes from the U, Th and K radioisotope content in a radius of about 25 cm around the quartz analyzed. Therefore, it is possible that the gamma dose has been slightly underestimated or overestimated, giving rise to very high uncertainty in the OSL dates compared to the ^{14}C results in LS. This is the reason why we are more confident in the radiocarbon age data to build the age model. However, the obtained OSL ages are statistically consistent among them and they point towards fast depositional (age-range overlapping) events giving rise to about 9.6 m of coarse sediments in less than 2.5 kyr. The high statistical errors due to the above-mentioned low sensitivity of the OSL signal in the studied sediments, fit with the proposed bayesian age-depth model providing an extrapolated age of ~ 18 cal kyr BP for the bottom of the LS-01 core (Fig. 3).

Sediment accumulation rates were calculated from the linear interpolation of AMS radiocarbon and OSL dates. SAR between the end of the core and 4.48 m (~18.0 to 15.7 cal kyr BP) was estimated for 4.21 mm/ yr. In the uppermost 4.48 m (15.7 to −65 cal yr BP) of the core, SARs

fluctuated between 0.05 and 0.86 mm/yr with a mean value of 0.28 mm/yr (Fig. 3).

4.2. Lithology, MS and organic geochemistry

4.2.1. Facies association and sedimentary features

Seven lithofacies (Gmg-1, Gmg-2, Gh, Dmc, B, Fm-1, Fm-2) are identified in the three stratigraphic records (LS-01, LS-02 and LS-03) (Fig. 4). Their stratigraphic distribution in the sediment core profiles is shown in Fig. 5. Each lithofacies is interpreted in terms of sedimentary processes as they are related to sedimentary transport mechanisms and/or processes of weathering and erosion in the source area. Different lithofacies representing analogue sedimentary processes have been grouped into four facies associations (FA1, FA2, FA3, FA4). Each facies association is related to a sedimentary (sub-)environment controlled by autogenic and/or allogenic (dominantly climate changes) factors. These sedimentary controls are discussed in section 5.

Facies association 1 (FA1): Debrites

This facies association consists of three lithofacies (Gmg-1, Gmg-2, Gh). It is located at the lowermost part of the three stratigraphic records constituting the stratigraphic U1 (Figs. 4 and 5). The synthetic MS reconstruction from the mean Z-scores was not fully representative of this unit since there was no clear lateral continuity between the different facies of this association (Fig. 5). A sharp top surface represented the vertical transition between FA1 and the overlying facies association (FA2 in all the cores) (Fig. 5).

Facies Gmg-1. This facies consists of a reddish matrix-supported gravel (conglomerate). The matrix was totally composed of sand with a coarse grain size between 0.5 and ~ 1 mm. The clasts showed sub-angular forms with low sphericity and an average grain size of ~ 1.5 cm. Inverse grading is observed in the lowest sections. This facies registers the lowest C/N (mean: 8.96 ± 0.61) in the record, very low TOC (mean: 0.5 ± 0.07 %) and high MS (mean: $2.4 \times 10^{-4} \pm 1.2 \times 10^{-4}$) values (Fig. 4).

Interpretation: Facies Gmg-1 could suggest cohesionless debris flows dominated by frictional grain interactions (Nemec and Steel, 1984).

Facies Gmg-2. This facies consists of a coarse-grained reddish matrix-supported gravel (conglomerate). The matrix is characterized by sand with a very coarse grain size (~2 mm). The clasts exhibited sub-rounded forms with low sphericity and an average grain size of ~ 2.2 cm. Inverse grading is observed. This facies records the lowest TOC in the record (mean: 0.46 ± 0.09 %), very low C/N (mean: 9.06 ± 1.57) and the highest MS (mean: $3.4 \times 10^{-4} \pm 5 \times 10^{-4}$) values (Fig. 4).

Interpretation: Facies Gmg-2 might be related to cohesionless debris flows dominated by frictional grain interactions. Inverse grading suggested mass freezing deposition as the driving shear stress drops at the slope foot (Sohn et al., 1999).

Facies Gh. This facies consists of reddish matrix to clast-supported gravel (conglomerate) with a crudely horizontally bedded marked by preferred subhorizontal clast orientation. The clasts were imbricated and showed rounded forms with low sphericity an average grain size of ~ 1.8 cm. This facies registers very high values of MS with a mean value of $2.6 \times 10^{-4} \pm 1.4 \times 10^{-4}$ (Fig. 4).

Interpretation: The well-developed parallel-to-bedding clast alignment and lacking of vertical clast alignment, large floating or protruding clasts could suggest incremental aggradation of the debris flows that experienced full laminar shear before deposition (Sohn et al., 1999). Subhorizontal preferred clast orientation is commonly originated parallel-to-flow from strongly sheared laminar flow due to clast interactions and dispersive pressure (Nemec and Steel, 1984).

Facies association 2 (FA2): Diamicton

Facies Dmc. This facies is dominated by well-developed stratification (banding or zonation) of alternating debris-poor and debris-rich layers with poorly-sorted angular clasts embedded in dark grey clay-matrix. It is classified as a clast-rich (5–50 %), muddy matrix-supported diamicton, following non-genetic of poorly-sorted sediment classification from Hambrey and Glasser, (2012). The matrix was characterized by a grain size lower than 0.004 mm. The clasts showed an average grain size of ~ 1.5 cm and commonly tabular morphology with horizontal a-axis. Scattered clasts appeared with a-axis vertically oriented. This facies records intermediate TOC (mean: 0.74 ± 0.22 %) and MS (mean: $1.9 \times 10^{-4} \pm 5.6 \times 10^{-5}$) values. The C/N ratio exhibits very high values (mean: 13.86 ± 5.13). The synthetic MS reconstruction from the mean Z-scores records intermediate values (Figs. 4 and 5).

Interpretation: The bi-modal ('pebble clay'-type fabric) with elongated particles subhorizontally aligned is commonly found on the glacigenic deposits (till) and also in nivation sediments (Menzies et al., 2006). Structureless, unpacked and poorly developed fabric of mostly angular clasts is common sedimentary features of supra-glacial tills or frost-shattered clasts fallen to nivation hollows (Bennett and Glasser, 2009). Fine grained matrix would represent the subglacial or sub-nivation basal melt layer where the supraglacial/supranival clasts were dropped and embedded into melting clays during the warmer season.

Facies association 3 (FA3): Breccia

Facies B. It consists of chaothic (non-graded), poorly-sorted and bimodal grain size (rough-sphericity quartzite pebbles and disc-shape schist microgranules) breccias, lacking a fine-grained matrix. The clasts informed sub-angular forms with low sphericity and an average grain size of ~ 1.4 cm. This facies records very low MS (mean: $7.3 \times 10^{-5} \pm 4.3 \times 10^{-5}$) values (Fig. 4). The synthetic MS reconstruction from the mean Z-scores are not fully representative due to facies B is only recorded in LS-03 (Fig. 5).

Interpretation: The angular morphology of clast and the lack of matrix supporting them (in contrasting with FA1) suggest this facies is a slope-base accumulation of clasts from frost shattering bedrock. Different lithology in bedrock (quartzites and schists) controlled the heterogeneity of grain size and clast-morphology. This local deposit, not registered in cores LS-01 and LS-02, was triggered by a low-efficiency transversal transport mechanism.

Facies association 4 (FA4): Lutites

Facies Fm-1. This facies consists of a massive grey mudstone with a grain size less than 0.004 mm. This facies registers the lowest mean values of MS ($6.9 \times 10^{-5} \pm 2.1 \times 10^{-5}$) and the highest of TOC (1.53 ± 1.83 %) and C/N (14.92 ± 2.38) of the record. The synthetic MS reconstruction from the mean Z-scores also records the lowest values in the sedimentary record (Figs. 4 and 5).

Interpretation: Facies Fm-1 were deposited by suspension settling of clays into standing water.

Facies Fm-2. This facies consists of a massive brown mudstone with a grain size less than 0.004 mm. This facies registers very low mean values of MS ($1 \times 10^{-4} \pm 4.4 \times 10^{-5}$) and C/N ($10.84 \pm 1.61$), and high of TOC ($1.44 \pm 1.8$ %). The synthetic MS reconstruction from the mean Z-scores records low values (Figs. 4 and 5).

Interpretation: Facies Fm-2 were deposited by suspension settling of clays into standing water.

4.2.2. Stratigraphic units

Three stratigraphic units (U1, U2 and U3) in LS cores LS-01, LS-02 and LS-03 were defined by lithology (colour changes and visible textural differences) and MS, TOC and C/N data (Fig. 5). The macroscopic distinction of these units was supported by marked changes in MS (mean MS values from LS-01, LS-02 and LS-03), TOC and C/N values. TOC and C/N data were obtained only for LS-01.

The unit 1 (U1) constituted the basal unit in cores LS-01 and LS-03

with a thickness of 1.4 m and 1.7 m, respectively. This unit was not represented in LS-02. The real thickness of U1 is unknown because none of the cores reached the bedrock. The U1 was composed of conglomerates and registered the lowest mean values of TOC and C/N (0.47 ± 0.09 % and 9.04 ± 1.46, respectively) and the highest mean MS (3.1 × 10^{-4} ± 4.2 × 10^{-4}). The synthetic MS reconstruction from the mean Z-scores exhibited the highest values in the sedimentary record. The contact with the overlying unit was sharp (Fig. 5).

The unit 2 (U2) was represented in the three studied cores. The U2 thickness was 4.1 m in LS-02, 8.2 m in LS-01 and 3.1 m in LS-03. The U2 is not fully represented in LS-02 due to the shallow depth drilled in this location. The U2 was composed of angular clasts embedded in clays and registered intermediate values of TOC, MS and synthetic MS reconstruction from the mean Z-scores. The C/N ratio exhibited the highest mean values in the sedimentary record. Values for U2 are the same as the ones in FA2, previously detailed in the section 4.2.1. An abrupt change is observed in the sedimentation rate between this unit and the overlying one, fluctuating from 4.21 to 0.28 mm/yr (Fig. 3). The contact with the overlying unit was sharp (Fig. 5).

The unit 3 (U3) was also represented in the three cores with thickness of 5.5 m in LS-02, 4.5 m in LS-01 and 3.3 m in LS-03. This unit was principally composed by clays and registered the highest mean values of TOC (1.48 ± 1.8 %) and lowest MS (9.1 × 10^{-5} ± 4.2 × 10^{-5}) of the studied sediment cores. The C/N ratio registered intermediate mean values (12.46 ± 2.79). The synthetic MS reconstruction from the mean Z-scores exhibited the lowest values in the sedimentary record (Fig. 5).

5. Discussion

Laguna de Río Seco (LdRS) registers the oldest sedimentary record – the last ~ 12.3 cal kyr BP – retrieved from an alpine wetland in the Sierra Nevada recovered until now (Anderson et al., 2011; Jiménez Espejo et al., 2014; Toney et al., 2020). Therefore, previously there has been a lack of information about the paleoenvironmental history of these alpine wetlands during the deglaciation. The sedimentological and paleoenvironmental record of Laguna Seca, which covers the last ~ 18.0 cal kyr BP, sheds light on this period in the Sierra Nevada and provides valuable paleoenvironmental information about the response of these alpine wetlands to the regional and global paleoclimatic changes since the end of the last glacial cycle. Three main paleoenvironmental stages can be identified in the LS setting from the deglaciation to the Holocene: (1) a paraglacial stage dominated by mass flows, (2) a small glacier or nivation hollow stage and (3) a lacustrine stage between ~ 15.7 cal kyr and the present (Figs. 6 and 7). This final stage is interrupted by a periglacial substage, probably during the YD. Additionally, the features of the first paraglacial stages and previous studies of landforms in LS basin would point towards the presence of a previous small glacier cirque, lacking till or glacier depositional morphologies, that sculpted the head of the basin during the Last Glacial Maximum.

5.1. Paraglacial stage

This stage is recorded by debrites (FA1) deposited from cohesionless debris flows. Their reddish matrix supports a subaerial setting for these mass flow conglomerates (Figs. 4, 5, 6j and 7a). An increase in textural maturity in debrites (i.e., decreasing of grain size) from core LS-1 to LS-3 indicates a west (proximal) to east (distal) flow direction along an axial system (SW-E) coming from the eastward slope of Chullo peak (Fig. 1c, d and 5). Debrites are not recorded in core LS-2 as this stratigraphic horizon is deeper than LS-2 drilled depth (Fig. 5). Proximal to distal facies changes in short distances (e.g., from Gmg-lithofacies in LS-1 to Gh-lithofacies in LS-3 in a distance of ~ 50 m) indicate rapid changes in flow rheology (Fig. 1d and 5) triggered by the pre-debrite topography sculpted into the basin bedrock. Slope bedrock lithology (schists and quartzite), short distance (above 500 m) of the alluvial system between the source area (slope) and the sink (LS cirque/hollow floor), combined

with the poor grain interactions that occurred into debris flows do not justify the relatively high roundness of the debrite clasts (Fig. 1c, d and 4). The recycling of sediments from previous deposits in the slopes and/ or a previous period of high-intensity weathering that affected the bedrock in the slopes would explain the activity of debris flows as the main slope sediment transport mechanism and the relatively high textural maturity of the debrite clasts.

Slope was presumably the most important topographic factor controlling the flows. In fact, currently an important slope of 9.9° is observed in the transect SW-E in the LS basin (Fig. 1c and d). However, climatic control should also have played an important role not only during the debris flow phase but also during the preceding period. A pre-debrite glacial period (LGM) could have prepared the slopes (i.e., steepened rockwalls) and also generated drift-mantled slopes (i.e., talus debris resting against the slope) that could have been reworked by debris flows during the subsequent paraglacial period. Sierra Nevada registered important glacier advances at the end of the LGM and during HS1 that probably reached ~ 2000 masl on the north faces (Palacios et al., 2016). Therefore, the LS catchment is located in an optimum elevational range (from ~ 2259 to 2540 masl) for glacier activity during these periods.

Debris flow is the main erosional to transport mechanism reworking sediment-mantled slopes in recent (and deglaciation period) paraglacial settings (Ballantyne et al., 2002). Additionally, high debris-flow activity occurs on slopes during intense rainfall periods (high water availability), especially after arid periods, when slopes are favored by high soil moisture due to snowmelt during deglaciation (Zimmermann and Haeberli, 1992; Palacios et al., 1999; Sletten et al., 2003). The glacier advances registered in Sierra Nevada at ~ 20–19 cal kyr BP were followed by a major deglaciation (Oliva et al., 2014; Palacios et al., 2016). This intense melting could have triggered the instability processed that gave rise to the described debris flows at the bottom of the LS record. This glacial regression was also observed in other Iberian locations such as the Central Range (Pedraza et al., 2013) and the Pyrenees (Serrano et al., 2015) suggesting milder (temperate and humid) climate conditions. Low values of xerophytes in the Padul wetland before ~ 18.4 cal kyr BP (Camuera et al., 2021) and a stable temperature pattern of around 13.5 °C from Alboran Sea (Martrat et al., 2014) could be also coherent with a moderate increase in precipitation and temperature in the western Mediterranean region at this time (Fig. 6d and c).

The sedimentation rate for this paraglacial stage in LS was estimated in 4.21 mm/yr on the basis of a minimum debrite thickness of ~ 1.5 m (drilling did not reach the bedrock), probably deposited in less than ~ 350 years (Figs. 3 and 5). A combination of factors like sediment availability, lack of terrestrial vegetation (deduced from the lowest % TOC and C/N values in the record; Fig. 6e and f) and slope instability (high detrital input showed by the highest synthetic MS reconstruction from the mean Z-scores; Fig. 6g), enhanced the geomorphic activity giving rise to high sedimentation rates in these debris-flow-dominated paraglacial settings during the initial stages of the deglaciation (Fig. 7a).

The occurrence of post-LGM paraglacial debrites along with the elevational range of glacier development in the Sierra Nevada suggest that the potential origin of the present LS basin could have been a relict glacial cirque sculpted during the LGM. This hypothesis would agree with a previous study that suggested a first and undated cold episode that formed a glacial cirque at 2370 masl in the LS catchment (Simón et al., 2000; Fig. 2). However, sediment sources (glacially-conditioned sediment availability) for paraglacial debris flows could have been drift-mantled slopes accumulated in the LS basin until 2540 masl (Fig. 1c). The paraglacial term was initially used for 'a period of rapid environmental adjustment following glacier retreat' (Benn and Evans, 2010). Paraglacial processes (i.e., slope adjustment by slope-failures, till reworking by debris flow and so on) occur rapidly from centuries (it is observed over the last 200 years in areas with glaciers retreated since the LIA, Serrano et al., 2018) to millennia. This timing for paraglacial processes fits well with the time lapse (1 to 5 kyr) between the hypothetic
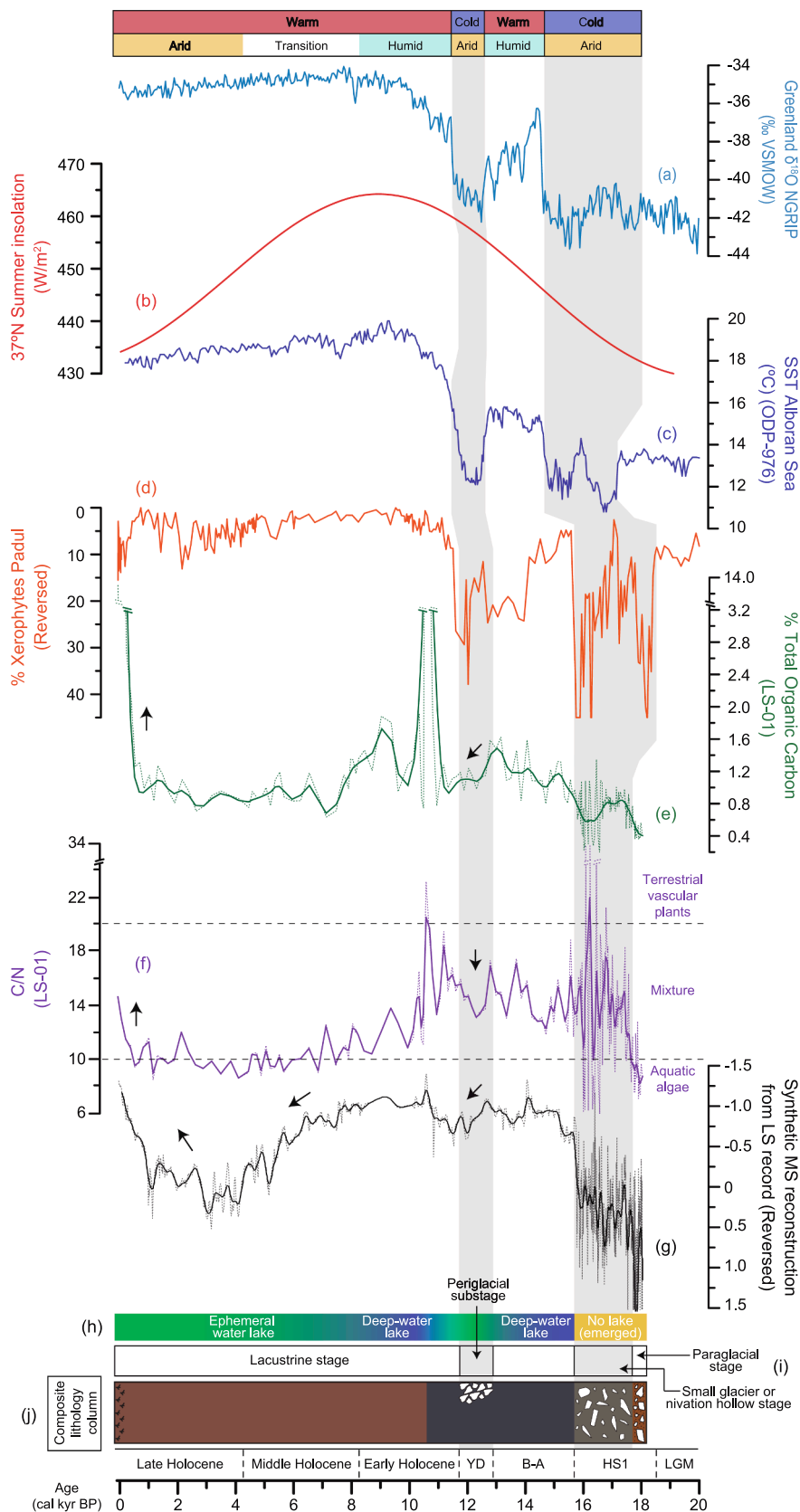
Fig. 6. (a) δ¹⁸O values of the NGRIP ice core from Greenland (North Greenland Ice Core Project Members, 2004) (b) Summer insolation calculated for 37°N (Laskar et al., 2004) (c) Sea Surface Temperature (SST, °C) from ODP-976 record of Alboran Sea (Martrat et al., 2014) (d) Percentage of xerophytes from Padul-15–05 record (values inverted) (Camuera et al., 2019, 2021) (e) Percentage of total organic carbon from LS-01 record (dashed line) (f) C/N ratio from LS-01 record (dashed line) (g) Synthetic MS reconstruction from the mean Z-scores of magnetic susceptibility from LS sedimentary record (LS-01, LS-02 and LS-03) (dashed line). Smoothed spline function with a smooth value of 6.5 was used to facilitate the comparison of %TOC, C/N and synthetic MS data with other proxies (continuous line of 6e, f and g) (h) Estimated lake level of LS (i) Different paleoenvironmental stages registered in LS (j) Composite lithology column from LS sedimentary record (LS-01, LS-02 and LS-03). Grey bars represent cold and arid periods (HS1 and YD). Acronyms: LGM; Last Maximum Glacial, HS1; Heinrich Stadial 1, B-A; Bølling-Allerød, YD; Younger Dryas.
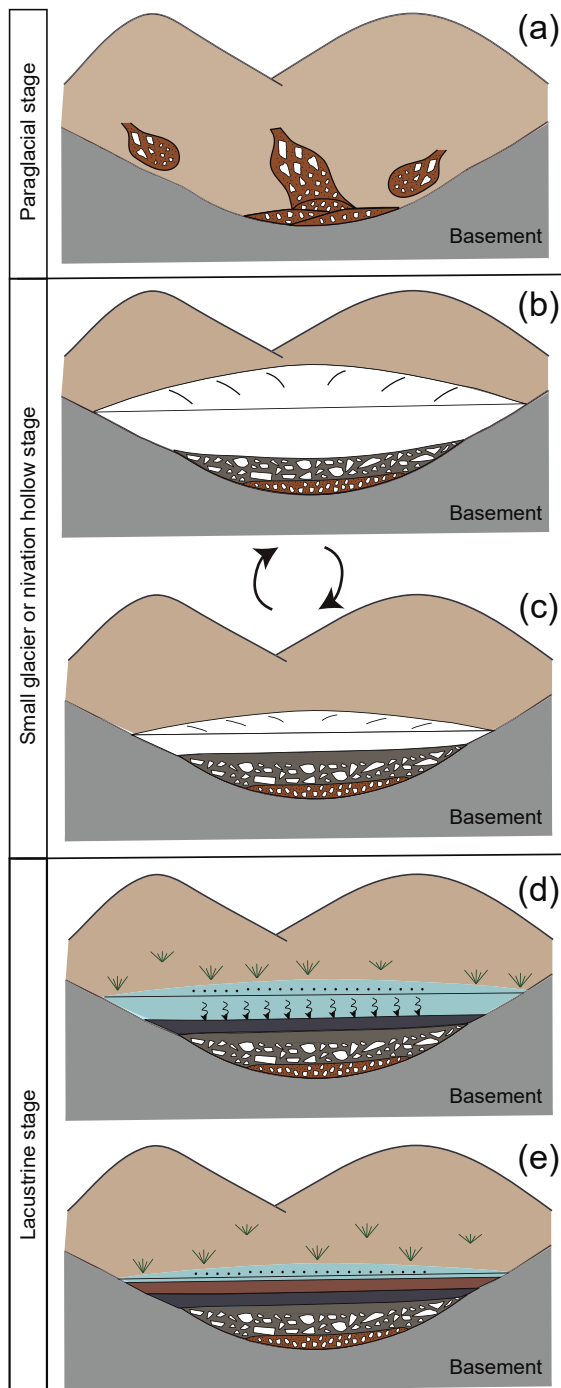
Fig. 7. Schematic representation of the different paleoenvironmental stages from LS with respect to sedimentological features, MS, TOC and C/N data. Three principal stages are differentiated: paraglacial stage dominated by mass flows, small glacier or nivation hollow stage and lacustrine stage. (a) The paraglacial stage is dominated by subaerial cohesionless debris flows. (b, c) The small glacier or nivation hollow stage is dominated by glaciogenic deposits (till) or nivation sediments. Deposits fluctuate depending on seasonal climate oscillations: (b) winter frost-shattered of the nivation free bedrock scarps and clasts fall into the snowpatch or (c) nivation summer melt with clay layer deposition and embeded clasts. (d, e) A lacustrine stage dominated by suspension settling of clays into standing water in a deep (d) and ephemeral lake (e).

glacier till developed in a glacier cirque stage during the LGM (23–19 cal kyr BP) and the paraglacial debrite (~18 cal kyr BP) in LS (Fig. 6j).

The location of the LS cirque in the lee of southwestern prevailing winds presumably protected the snow accumulation, limiting deflation (Fig. 1c). In addition, this basin was probably a trap for the snow blown from the west windward slope. The tendency for mid-latitude cirques to face eastward is considered to reflect the glacier growth and survival in the lee of westerly winds that dominate at these latitudes (Benn, 1989). The cirque floor altitude of 2259 masl in LS or the ratio between cirque threshold and cirque headwall altitudes between ~ 2300 and ~ 2500 masl, respectively, in LS, have been used as a proxy of glacier's ELAs for former periods of glaciations (Principato and Lee, 2014; Mitchell and Humphries, 2015). This ELA estimation method is well-fitted when glaciers were comparatively small and confined into their cirques (Evans, 1999), as occurred in Sierra Nevada just after the LGM when the glaciation was marginal (Oliva et al., 2014; Palacios et al, 2016). On the basis of the till/nivation deposits preserved in LS, the palaeo-ELA can be estimated at above ~ 2400 masl during the LGM (23–19 cal kyr BP), which is in accordance to the ELA estimated for Sierra Nevada by atmospheric reconstructed modeling (between 2400 and 2600 masl, Kuhlemann et al., 2008) and based on geomorphological evidences (Oliva et al., 2014).

5.2. Small glacier or nivation hollow stage

This stage is represented by facies association FA2 that is interpreted as glacially-derived till diamicton or diamicton derived by snowpatch-related nivation hollow (Figs. 4, 5, 6j, 7b and c). A combination of contemporary periglacial processes could explain the bi-modal diamicton in LS: (1) winter frost-shattered of the nivation free bedrock scarps and clasts fall into the snowpatch (Fig. 7b) and (2) nivation summer melt and a clay layer deposited embedding clasts (Fig. 7c). Therefore, this facies deposits occurred most likely due to seasonal climate oscillations under a generally cold and arid conditions. The clasts were product of frost shattering physical weathering processes, hence their angular nature (Fig. 4). The temperature would have increased during the warm season producing the snow/ice melting, and would generate the remobilization of the shattered material downslope to the depocentre of the basin. Evidences of significant run-off in the LS basin is deduced by high values of the synthetic MS reconstruction from the mean Z-scores (Fig. 6g). Probably, run-off linked to seasonal climate oscillations would explain the variability in the contribution and origin of the organic matter in this facies. The low %TOC and the important variation in the C/N values, which oscillate from 5.3 to 33.5, suggest low productivity with a mixture source between terrestrial (C/N values above 20 that indicate the predominance of vascular plants; Meyers, 1994) and microbial (C/N values lower than 10 probably indicate the presence of bacteria and/or algae; Tyson, 1995; Meyers, 1994, 2003) organic matter (Fig. 6e and f).

Very cold and arid climate conditions in the western Mediterranean between ~ 17.7 and 15.7 cal kyr BP probably led the deposit of the diamicton in LS and important environmental changes in other locations from this region (Bard et al., 2000; Fletcher and Sánchez-Goñi, 2008; Combourieu-Nebout et al., 2009; Carrión et al., 2010; Fletcher et al., 2010; Moreno et al., 2012). In southern Iberia, the nearby sedimentary record from Padul wetland registered a decrease in mesic forest and an increase in xerophytes reaching maximum values, suggesting very dry conditions (Camuera et al., 2021) (Fig. 6d). In addition, the ODP-976 record from the Alboran Sea also showed a sharp drop in the sea surface temperature (SST) during this period, reaching the lowest values from the last 20 cal kyr BP (Martrat et al., 2014) (Fig. 6c). These climatic conditions and environmental changes are also registered in other locations from the northern Iberian Peninsula such as the Lake Estanya where shallow lake levels, saline waters and reduced organic productivity reached their maximum values between 18 and 14.5 cal kyr BP (Morellón et al., 2009). These environmental features in the western

Mediterranean region favored a major glacier advance that refilled the high-elevation valley bottoms in Sierra Nevada at ~17.5 cal kyr BP (Palacios et al., 2016). This fact agrees with the presence of moraines in the Iberian Central Range (Andrés y Palacios, 2014; Carrasco et al., 2015) and in the Pyrenees (Delmas et al., 2008; Pallás et al., 2010; Palacios et al., 2015a; Palacios et al., 2015b; Turu et al., 2016) between 17.5 and 14.5 cal kyr BP, indicating that deglaciation was interrupted by cold conditions and glaciers readvanced significantly in many mountains in Iberia. In fact, glaciers also advanced in some areas in northern Europe without reaching the previous extension of the LGM (Ivy-Ochs et al., 2009; Giraudi, 2015; Ivy-Ochs, 2015; Makos, 2015), as well as small glacier cirques in other *peri*-Mediterranean massifs at similar latitude such as the mountains of the Balkans and Greece (Leontaritis et al., 2020; Allard et al., 2020).

5.3. Lacustrine stage (15.7 cal kyr BP - present)

This stage is represented by FA3 and FA4. Facies association 3 is interpreted as frost-shattering breccia deposited in a periglacial substage, representing a short period during a lacustrine stage (Figs. 4, 5 and 6j). Facies association 4 are interpreted as suspension settling mudstone into standing water during a lacustrine stage (Figs. 4, 5, 6j, 7d and e). Two different facies are differentiated in FA4: (1) Facies Fm-1 are interpreted as a deep-water lacustrine stage under overall humid conditions and probably linked with an ice-melting caused by an important increase of temperatures in Sierra Nevada (Fig. 6h, i, j and 7d) and (2) Facies Fm-2 are interpreted as an ephemeral water lacustrine stage under an overall long-term aridification trend (Fig. 6h, i, j and 7e). Both mudstone facies are characterized in general terms by high organic matter and low detrital content (Fig. 6e and g).

The grey mudstone facies (Fm-1) presents the highest organic matter content (highest %TOC values), with a mixture contribution of terrestrial vascular plants and aquatic algae (C/N values between 10 and 20, with a mean of ≃15; Meyers, 1994), and the lowest detrital content (lowest values of the synthetic MS reconstruction from the mean Z-scores) from the LS sedimentary record (Figs. 4, 6e, f and g). These factors along with the absence of clasts would indicate a warmer and more humid climate compared to previous stages. The abrupt facies change observed at ~ 15.7 cal kyr BP suggests a major change in the paleoclimatic and paleoenvironmental conditions in the Sierra Nevada. According to Palacios et al. (2016), the glaciers in Sierra Nevada receded and probably disappeared during the Bølling-Allerød (B-A). This rapid glacier retreat was also registered in the central Iberian Peninsula (Palacios et al., 2011, 2012), in the north-west mountain ranges (Fernández-Mosquera et al., 2000; Cowton et al., 2009) and in the Pyrenees (González-Sampériz et al., 2006; Pallàs et al., 2006, 2010; Delmas et al., 2008; Sancho et al., 2008) between 16 and 15 cal kyr BP. The limit between the diamicton (cold/arid conditions) and the grey mudstone (warm/humid conditions) of the LS sedimentary record agrees in time with an important drop in the xerophyte content observed in the Padul wetland pollen record at the beginning of the B-A (~15.7 cal kyr BP) (Fig. 6d). Camuera et al. (2021) observed an expansion of the Mediterranean forest induced by a significant increase in precipitation, coeval with an important increase in SST temperatures in the Alboran Sea (Martrat et al., 2014) (Fig. 6d and c). This temperature rises in southern of Iberian Peninsula was probably controlled, among other factors, by a northern Hemisphere summer insolation increase (Laskar et al., 2004), that would also have triggered significant ice-melting in Sierra Nevada forming a relatively deep-water lake in the LS basin (Fig. 6b, c and 7d).

The breccia facies (FA3) was only registered in the LS-03 record, the most distal of the three cores (Figs. 4 and 5). This facies deposit is interpreted as an occasional slope-base accumulation of clasts from frost-shattering bedrock processes in the southeastern reliefs, linked with a periglacial substage that could have been linked to the YD (Fig. 1c, 2, 6i and j). Gelifraction lobes have been described at the base of

the southeastern slope of the LS basin, where the slope is very steep (Simón et al., 2000; Fig. 1c, e and 2). These gelifraction lobes flowed into the main axial system (SW-E) and, according to Simón et al. (2000), could have been linked with an undated last cold episode, periglacial rather than glacial, that affected environments and sedimentation in LS. The spatial distribution and small-scale of the gelifraction lobes would justify the lack of this deposit in the LS-01 and LS-02 cores located 50 m further to the west, where lacustrine sediments accumulated instead (Fig. 1c, 2, 5 and 6j). Although there is no age control for LS-03 core, the chronostratigraphic correlation between LS-01 and LS-03 would allow for inferring the approximate age of the breccia deposit between ~ 15.6 and 10.6 cal kyr BP (Fig. 5). However, since this deposit is stratigraphically closer to the overlying radiocarbon date at the bottom of brown mudstone – Fm-2 – (~10.6 cal kyr BP) in LS-01 core, it could coincide in time with the YD (from ~ 12.9 to 11.7 cal kyr BP). Laterally-equivalent lacustrine sediments showed a drop in organic matter, composed principally by a mix between terrestrial vascular plants and aquatic algae, and an increase in detrital content, suggesting cold and dry climatic conditions and probably a lowering of the lake level that could have ended up with the emersion of core LS-03 after the breccia deposition (Fig. 6e, f, g and h). During this period, small glaciers developed again in Sierra Nevada but only at high-altitude cirque basins with specific orientations (Palacios et al., 2016), as response to the global cold and dry atmospheric conditions (see low values of Greenland NGRIP δ^{18}O ice record; Fig. 6a). Local pollen studies at lower elevation in the Sierra Nevada exhibit relative high content of xerophytes during the YD indicating cold and arid conditions (Fig. 6d; Camuera et al., 2021). An *Artemisia-Ephedra* pollen signal paralleling a forest depletion is also visible during the YD at 225 masl in the eastern Iberia sequence of Navarrés (Carrión and van Geel, 1999). At a broader scale, these findings are in tune with an abrupt and pronounced drop in the temperate forest signal in the western Mediterranean (Fletcher et al., 2010). Both xerophytic development and temperate forest decline were linked to a rapid vegetation response to aridity and low temperature in the western Mediterranean during the YD (Fletcher et al., 2010; Martrat et al., 2014) (Fig. 6c). In addition, the probably lowering lake level of LS at this time would be in tune with the behavior of other mid-European lakes that during the early and late stages of the YD showed high lake-levels with a middle phase of lake-level lowering (Magny, 2001; Magny et al., 2006).

After the YD and up to ~ 10.6 cal kyr BP, LS registered continuous sedimentation of facies Fm-1 in the deepest areas of the basin (represented in both LS-01 and LS-02 records) with a very high content of organic matter from a mix between terrestrial vascular plants and aquatic algae (Fig. 6e, f, i and j). However, facies Fm-1 did not overlie facies B in core LS-03 (Fig. 5), likely related to an occasional emersion of this part of the basin. This would suggest that lake-level would have remained low during the YD-Early Holocene transition (Fig. 6h). After the YD, glaciers in Sierra Nevada started retreating towards their valley heads until they completely disappeared (Palacios et al., 2016). During this time, the nearby sedimentary record from Laguna de Río Seco registered clays rich in organic matter, with significant *Botryococcus* colonies and steppe vegetation pollen taxa that would probably indicate an important input of nutrients and suggesting similar relatively cold and dry environmental conditions as LS (Anderson et al., 2011). In fact, the facies change from grey to brown mudstone (from Fm-1 to Fm-2) and the highest organic matter content (from terrestrial vascular plant source) observed in LS during the Early Holocene (~10.6 cal kyr BP; Fig. 6e, f and j), coincides in time with the start of decline in steppe and occurrence of the more mesic tree and shrub species from Laguna de Río Seco (Anderson et al., 2011) suggesting a shift towards more warm and humid conditions. Higher lake levels conditions recovered in LS at that time. These environmental and climate conditions are also observed in other records from the southern of Iberian Peninsula (i.e., in the decreasing trend of xerophytes content from the Padul wetland; Fig. 6d) and the Alboran Sea (i.e., in the increasing trend of sea surface temperature; Fig. 6c).

The brown mudstone facies (Fm-2) presents a decreasing trend in the organic matter content, with a transition in the organic matter source towards aquatic algae, and an increasing trend in the detrital content that can be interpreted as a primary productivity decline and more detritic inputs in the LS catchment throughout the Holocene (Fig. 6e, f and g). These features indicate a transition from a warm and humid climate during the Early Holocene (after 10.6 cal kyr BP) to warm and generally arid conditions from the Middle Holocene to the present, which would generate a change in the LS water level from a deep-water to an ephemeral lake (Fig. 6h, 7d and e).

During the Early Holocene (between ~ 10.6 and 8.2 cal kyr BP), the Fm-2 facies registered the highest values of organic matter, with a mixture contribution of terrestrial vascular plants and aquatic algae, and the lowest detrital content of the sedimentary record suggesting a deep-water lake level in LS and the warmest and wettest conditions of the Holocene (Fig. 6e, f, g, h and 7d). The onset of more humid conditions in LS started at ~ 10.6 cal kyr BP (Fig. 6e, f and g). These climate conditions modulated the paleoenvironments, principally the accumulation of organic matter and regional vegetation, as can be seen in many other records from Sierra Nevada such as Laguna de Río Seco (Anderson et al., 2011) and Padul wetland (Ramos-Román et al., 2018a).

Between the Middle and Late Holocene (from ~ 8.2 cal kyr BP until the present), the Fm-2 facies registered lower organic matter content and mostly deriving from aquatic algae (C/N values below 10; Meyers, 1994), and a significant increasing trend in detrital content in the LS catchment (Fig. 6e, f and g), suggesting a general long-term aridification trend that has been observed in several records from Sierra Nevada (Anderson et al., 2011; Jiménez-Moreno and Anderson, 2012; Ramos-Román et al., 2018a; Ramos-Román et al., 2018b; Jiménez-Espejo et al., 2014) and in other sites from western Mediterranean (Fletcher and Sánchez-Goñi, 2008; Combourieu-Nebout et al., 2009; Carrión et al., 2010; Rodrigo-Gámiz et al., 2011). The gradual environmental change towards more regional aridity that became enhanced at around ~ 6 cal kyr BP in LS and other records from the Sierra Nevada (Jiménez-Espejo et al., 2014; Jiménez-Moreno et al., 2020) agrees in the timing of the termination of the African Humid Period at ~ 6 cal kyr BP (deMenocal et al., 2000) and the establishment of the current atmospheric dynamics in southern Iberia (Toney et al., 2020; García-Alix et al., 2021), indicating synchronicity in the North Atlantic Ocean-atmospheric dynamics and orbital forcing with the decrease in summer insolation as main climate driver in the western Mediterranean and northern Africa. Under this scenario LS evolved from a deep-water into an ephemeral lake with important aquatic productivity in the Middle-Late Holocene transition, developing late summer desiccation in the last centuries (Fig. 6f, h, 7d and e). This aridification trend was most likely related to a reduction in winter precipitation due to decreasing summer insolation (Magny et al., 2012; Fig. 6b), modulating the accumulation of organic matter and transforming the vegetation in the Sierra Nevada alpine environments with the reduction of forested species. This is observed in nearby sedimentary records such as Laguna de Río Seco (Anderson et al., 2011), Borreguiles de la Virgen (BdlV; Jiménez-Moreno and Anderson, 2012) and the Padul wetland (Ramos-Román et al., 2018b), and in different sites from western Mediterranean area (Carrión, 2002; Carrión et al., 2010; Fletcher and Sánchez-Goñi, 2008; Jalut et al., 2009; Fletcher et al., 2013; Jiménez-Moreno et al., 2015).

The sedimentary infilling, and thus, the reduction of the accommodation space in the basin, could have been one of the factors that forced the Middle-Late Holocene shallowing of LS (Fig. 6h and 7e). Closed lake systems in alpine regions with small catchment basins have low potential for sediment accumulation since the mechanical denudation and detrital sedimentation are directly related to drainage/lake area ratio, in addition to lithology and climate (Einsele and Hinderer, 1997). Depending on these factors, the alpine lakes could become filled up in several hundreds or thousands of years (Einsele and Hinderer, 1997). In the case of LS, although the catchment area only covers ~ 58.8 ha, the reduced area for sediment accumulation gave rise to almost ~ 12 m of

sedimentary deposits from ~ 18 to ~ 6 cal kyr BP, reducing the potential volume of the basin (Fig. 1c, 5 and 7e). However, according to the topography, LS lake level could be higher than the current 0.5 m in late spring since the outflow of this endoreic basin is located ~ 15 m above the present depocentre (Fig. 1c). This would mean that although the contribution of the basin infilling to the reduction of the water level was significant, the general aridification trend registered from the Middle Holocene until the present in the western Mediterranean has been the main driver controlling the lake level in LS (Fig. 6e, f, g, h and 7e).

The last ~ 500 cal yr BP of the LS record, represented by the Fm-2 facies, are characterized by the highest content of organic matter for the entire sedimentary sequence (Fig. 6e). This organic matter content and the C/N values suggest a simultaneously significant accumulation of algae and terrestrial vascular plants (Fig. 6e and f) that could have been anthropically-forced (lake eutrophication and/or soil erosion in the catchment). A trend in increasing human activity in the last centuries is observed in other surrounding wetland records, such as the Laguna de la Mosca (Oliva and Gómez-Ortiz, 2012), Borreguil de la Virgen (García-Alix et al., 2017) or Borreguil de los Lavaderos de la Reina (López-Avilés et al., 2021). In fact, there are multiple evidences in Sierra Nevada of disturbance in the natural distributions of some plant species linked to reforestation (Anderson et al., 2011; Jiménez-Moreno and Anderson, 2012), as well as records of grazing activities or cultivation (Ramos-Román et al., 2019) and atmospheric pollution (García-Alix et al., 2017), that reveal an important human footprint during the last centuries.

6. Conclusions

The LS alpine wetland is at a key latitude and altitude in the western Mediterranean region, containing a highly sensitive sedimentary archive of the paleoenvironmental changes since the last deglaciation. The sedimentological, chronological, MS, TOC and C/N datasets obtained from the LS sedimentary record show that:

1. The core LS-01 is the longest and oldest record retrieved in alpine Sierra Nevada areas, covering the last ~ 18 cal kyr BP and providing valuable paleoenvironmental and paleoclimatic information of previously unrecorded climatic periods such as the HS1, B-A or the YD in the largest mountain range in southern Iberia.
2. Four climatically-controlled facies associations, three coarse-grained gravel and one fine-grained sedimentary deposit, have been identified and interpreted in terms of transport mechanisms and paleoenvironments: (1) subaerial cohesionless debris flows during a paraglacial stage, (2) till or nival diamicton during a small glacier/nivation hollow stage, (3) massive mudstone by suspension settling of clays into standing water during a lacustrine stage from ~ 15.7 cal kyr BP to the present and; (4) frost-shattering breccia deposited inside the lacustrine stage, only in an area of the wetland, probably during the YD and related with a periglacial substage.
3. Paraglacial slope processes during the first deglaciation stages should have been linked to the availability of slope sediments with a glacial origin, supporting the development of a previous small glacier or cirque glacier (2300–2500 masl) in the LS basin during the LGM, and agreeing with the landforms in the catchment basin and confirming the LGM-ELA estimation from other external proxies and atmospheric circulation models above 2400 masl in Sierra Nevada.
4. The sedimentation rates obtained in the different climatically-controlled sedimentary units (4.21 mm/yr during the paraglacial and small glacier/nivation stage and 0.28 mm/yr during the lacustrine stage) confirm that the geomorphic activity was accelerated just after glaciers retreated in the Sierra Nevada mountain range, due to a slope adjustment and high availability of sediments glacially conditioned.
5. An abrupt change in paleoenvironmental and paleoclimatic conditions have been detected at ~ 15.7 cal kyr BP in LS probably related to an increase in summer insolation, temperatures and precipitation

in the western Mediterranean region. This scenario boosted a significant ice-melting and glacier retreat in the Sierra Nevada. This high-water availability in the alpine areas of Sierra Nevada is compatible with the development of a deep lake with an important organic matter contribution (mixture between terrestrial vascular plants and aquatic algae) in the LS basin until the end of the Early Holocene (except in the YD that probably the lake level was lower). The general long-term aridification trend observed from the Middle Holocene to the present in the western Mediterranean region triggered the evolution from deep to ephemeral lacustrine conditions with an increase of aquatic productivity in the LS basin that ended up with the current summer desiccation of the lake.

6. Significant organic matter sedimentation with both aquatic and terrestrial origin could reveal an anthropically-forced shift during the last ~ 500 cal yr BP as observed in other surrounding alpine wetlands during the last centuries.

Declaration of Competing Interest

The authors declare that they have no known competing financial interests or personal relationships that could have appeared to influence the work reported in this paper.

Acknowledgements

References

Allard, J.L., Hughes, P.D., Woodward, J.C., Fink, D., Simon, K., Wilcken, K.M., 2020. Late Pleistocene glaciers in Greece: A new 36Cl chronology. Quat. Sci. Rev. 245, 106528. https://doi.org/10.1016/j.quascirev.2020.106528.

Anderson, R.S., Jiménez-Moreno, G., Carrión, J.S., Pérez-Martínez, C., 2011. Postglacial history of alpine vegetation, fire, and climate from Laguna de Río Seco, Sierra Nevada, southern Spain. Quat. Sci. Rev. 30 (13-14), 1615–1629. https://doi.org/10.1016/j.quascirev.2011.03.005.

Andrés, N., Palacios, D., 2014. Las fases de deglaciación del Sistema Central y su significado paleoclimático, in: Arnáez, J., González-Sampériz, P., Lasanta, T., Valero-Garcés, B. (Eds.), Geoecología, cambio ambiental y paisaje. Consejo Superior de Investigaciones Científicas, Instituto Pirenaico de Ecología: Universidad de la Rioja, Logroño, 49–64.

Ballantyne, C.K., 2002. Paraglacial geomorphology. Quat. Sci. Rev. 21 (18-19), 1935–2017. https://doi.org/10.1016/S0277-3791(02)00005-7.

Bard, E., Rostek, F., Turon, J.L., Gendreau, S., 2000. Hydrological impact of Heinrich events into the subtropical northeast Atlantic. Science 289, 1321–1324. https://doi.org/10.1126/science.289.5483.1321.

Barr, L.D., Sapagnolo, M., 2015. Glacial cirques as palaeoenvironmental indicators: their potential and limitations. Earth-Sci. Rev. 151, 48–78. https://doi.org/10.1016/j.earscirev.2015.10.004.

Benn, D.I., Benn, D.I., 1989. Debris transport by Loch Lomond Readvance glaciers in Northern Scotland: Basin form and the within-valley asymmetry of lateral moraines. J. Quat. Sci. 4 (3), 243–254. https://doi.org/10.1002/jqs.3390040305.

Benn, D.I., Evans, D.J.A., 2010. Glaciers and Glaciation, second ed. Routledge, London. https://doi.org/10.4324/9780203785010.

Bennett, M., Glasser, N., 2009. Glacial Geology: Ice Sheets and Landforms, second ed. Wiley-Blackwell, Chichester, United Kingdom.

Blaauw, M., Christen, J. A., 2011. Flexible Paleoclimate Age-Depth Models Using an Autoregressive Gamma Process 457–474. https://doi.org/10.1214/11-BA618.

Brennan, B.J., 2003. Beta doses to spherical grains. Radiat. Meas. 37, 299–303. https://doi.org/10.1016/S1350-4487(03)00011-8.

Brown, J., Harper, J., Humphrey, N., 2010. Cirque glacier sensitivity to 21st century warming: Sperry Glacier, Rocky Mountains, USA. Glob. Planet. Change 74 (2), 91–98. https://doi.org/10.1016/j.gloplacha.2010.09.001.

Camuera, J., Jiménez-Moreno, G., Ramos-Román, M.J., García-Alix, A., Toney, J.L., Anderson, R.S., Jiménez-Espejo, F., Kaufman, D., Bright, J., Webster, C., Yanes, Y., Carrión, J.S., Ohkouchi, N., Suga, H., Yamame, M., Yokoyama, Y., Martínez-Ruiz, F., 2018. Orbital-scale environmental and climatic changes recorded in a new ~200,000-year-long multiproxy sedimentary record from Padul, southern Iberian Peninsula. Quat. Sci. Rev. 198, 91–114. https://doi.org/10.1016/j.quascirev.2018.08.014.

Camuera, J., Jiménez-Moreno, G., Ramos-Román, M.J., García-Alix, A., Toney, J.L., Scott Anderson, R., Jiménez-Espejo, F., Bright, J., Webster, C., Yanes, Y., Carrión, J.S., 2019. Vegetation and climate changes during the last two glacial-interglacial cycles in the western Mediterranean: a new long pollen record from Padul (southern Iberian Peninsula). Quat. Sci. Rev. 205, 86–105. https://doi.org/10.1016/j.quascirev.2018.12.013.

Camuera, J., Jiménez-Moreno, G., Ramos-Román, M.J., García-Alix, A., Jiménez-Espejo, F.J., Toney, J.L., Anderson, R.S., 2021. Chronological control and centennial-scale climatic subdivisions of the Last Glacial Termination in the western Mediterranean region. Quat. Sci. Rev. 255, 106814. https://doi.org/10.1016/j.quascirev.2021.106814.

Carrasco, R.M., Pedraza, J., Domínguez-Villar, D., Willenbring, J.K., Villa, J., 2015. Sequence and chronology of the Cuerpo de Hombre paleoglacier (Iberian Central System) during the Last Glacial Cycle. Quat. Sci. Rev. 129, 163–177. https://doi.org/10.1016/j.quascirev.2015.09.021.

Carrión, J.S., 2002. Patterns and processes of late quaternary environmental change in a montane region of southwestern Europe. Quat. Sci. Rev. 21 (18-19), 2047–2066. https://doi.org/10.1016/S0277-3791(02)00010-0.

Carrión, J.S., Van Geel, B., 1999. Fine-resolution Upper Weichselian and Holocene palynological record from Navarrés (Valencia, Spain) and a discussion about factors of Mediterranean forest succession. Rev. Palaeobot. Palynol. 106 (3-4), 209–236. https://doi.org/10.1016/S0034-6667(99)00009-3.

Carrión, J.S., Fernández, S., González-Sampériz, P., Gil-Romera, G., Badal, E., Carrión-Marco, Y., López-Merino, L., López-Sáez, J.A., Fierro, E., Burjachs, F., 2010. Expected trends and surprises in the Lateglacial and Holocene vegetation history of the Iberian Peninsula and Balearic Islands. Rev. Palaeobot. Palynol. 162 (3), 458–475. https://doi.org/10.1016/j.revpalbo.2009.12.007.

Castillo Martín, A., 2009. Lagunas de Sierra Nevada, ed. Universidad de Granada, Granada.

Cheng, H., Edwards, R.L., Broecker, W.S., Denton, G.H., Kong, X., Wang, Y., Zhang, R., Wang, X., 2009. Ice age terminations. Science 326 (5950), 248–252.

Clark, P.U., Dyke, A.S., Shakun, J.D., Carlson, A.E., Clark, J., Wohlfarth, B., Mitrovica, J. X., Hostetler, S.W., McCabe, A.M., 2009. The Last Glacial Maximum. Science 325 (5941), 710–714.

Combourieu-Nebout, N., Peyron, O., Desprat, S., Beaudouin, C., Kotthoff, U., Marrot, F., 2009. Rapid climate variability in the West Mediterranean during the last 25000 years from high resolution pollen data. Clim. Past 5, 503–521. https://doi.org/10.5194/cp-5-503-2009.

Cowton, T., Hughes, P.D., Gibbard, P.L., 2009. Palaeoglaciation of Parque Natural Lago de Sanabria, Northwest Iberia. Geomorphology 108, 282–291. https://doi.org/10.1016/j.geomorph.2009.02.007.

Delmas, M., Gunnell, Y., Braucher, R., Calvet, M., Bourlès, D., 2008. Exposure age chronology of the last glacial cycle in the eastern Pyrenees. Quat. Res. 69, 231–241. https://doi.org/10.1016/j.yqres.2007.11.004.

Denton, G.H., Anderson, R.F., Toggweiler, J.R., Edwards, R.L., Schaefer, J.M., Putnam, A. E., 2010. The Last Glacial Termination. Science 328 (5986), 1652–1656.

deMenocal, P., Ortiz, J., Guilderson, T., Adkins, J., Sarnthein, M., Baker, L., Yarusinsky, M., 2000. Abrupt onset and termination of the African Humid Period: rapid climate responses to gradual insolation forcing. Quat. Sci. Rev. 19 (1-5), 347–361. https://doi.org/10.1016/S0277-3791(99)00081-5.

Einsele, G., Hinderer, M., 1997. Terrestrial sediment yield and the lifetimes of reservoirs, lakes, and larger basins. Geologische Rundschau 86 (2), 288–310. https://doi.org/10.1007/s005310050141.

Evans, I.S., 1999. Was the cirque glaciation of Wales time-transgressive, or not? Ann. Glaciol. 28, 33–39. https://doi.org/10.3189/172756499781821652.

Fernandez Mosquera, D., Marti, K., Romani, J.R.V., Weigel, A., 2000. Late Pleistocene deglaciation chronology in the NW of the Iberian Peninsula using cosmic-ray produced ²¹Ne in quartz. Nucl. Instrum. Methods Phys. Res. B 172 (1-4), 832–837. https://doi.org/10.1016/S0168-583X(00)00339-6.

Fletcher, W.J., Sánchez-Goñi, M.F., 2008. Orbital and sub-orbital scale climate impacts on the vegetation of the W. Mediterranean basin during the last 48 000 years. Quat. Res. 70, 451–464. https://doi.org/10.1016/j.yqres.2008.07.002.

Fletcher, W.J., Sánchez-Goñi, M.F., Peyron, O., Dormoy, I., 2010. Abrupt climate changes of the last glaciation detected in a Western Mediterranean forest record. Clim. Past 6, 245–264. https://doi.org/10.5194/cp-6-245-2010.

Fletcher, W.J., Debret, M., Goñi, M.F.S., 2013. Mid-Holocene emergence of a low-frequency millennial oscillation in western Mediterranean climate: Implications for past dynamics of the North Atlantic atmospheric westerlies. Holocene 23 (2), 153–166. https://doi.org/10.1177/0959683612460783.

Galbraith, R.F., Roberts, R.G., Laslett, G.M., Yoshida, H., Olley, J.M., 1999. Optical dating of single and multiple grains of quartz from Jinmium rock shelter, northern Australia: Part I, experimental design and statistical models. Archaeometry 41 (2), 339–364. https://doi.org/10.1111/j.1475-4754.1999.tb00987.x.

Galbraith, R.F., Roberts, R.G., 2012. Statistical aspects of equivalent dose and error calculation and display in OSL dating: an overview and some recommendations. Quat. Geochronol. 11, 1–2. https://doi.org/10.1016/j.quageo.2012.04.020.

García-Alix, A., Jiménez-Moreno, G., Anderson, R.S., Jiménez-Espejo, F., Delgado Huertas, A., 2012. Holocene paleoenvironmental evolution of a high-elevation wetland in Sierra Nevada, southern Spain, deduced from an isotopic record. J. Paleolimnol. 48, 471–484. https://doi.org/10.1016/j.chemgeo.2014.03.001.

García-Alix, A., Jiménez-Espejo, F.J., Toney, J.L., Jiménez-Moreno, G., Ramos-Román, M.J., Anderson, R.S., Ruano, P., Queralt, I., Delgado Huertas, A., Kuroda, J., 2017. Alpine bogs of southern Spain show human-induced environmental change superimposed on long-term natural variations. Sci. Rep. 7 (1) https://doi.org/10.1038/s41598-017-07854-w.

García-Alix, A., Jiménez-Espejo, F.J., Jiménez-Moreno, G., Toney, J.L., Ramos-Román, M.J., Camuera, J., Anderson, R.S., Delgado Huertas, A., Martínez-Ruiz, Q., I.,, 2018. Holocene geochemical footprint from Semi-arid alpine wetlands in southern Spain. Sci. Data 5, 180024. https://doi.org/10.1038/sdata.2018.24.

García-Alix, A., Camuera, J., Ramos-Román, M.J., Toney, J.L., Sachse, D., Schefuß, E., Jiménez-Moreno, G., Jiménez-Espejo, F.J., López-Avilés, A., Anderson, R.S., Yanes, Y., 2021. Paleohydrological dynamics in the Western Mediterranean during the last glacial cycle. Glob. Planet. Change 202, 103527. https://doi.org/https://doi.org/10.1016/j.gloplacha.2021.103527.

García-Ruiz, J.M., Palacios, D., González-Sampériz, P., de Andrés, N., Moreno, A., Valero-Garcés, B., Gómez-Villar, A., 2016. Mountain glacier evolution in the Iberian Peninsula during the Younger Dryas. Quat. Sci. Rev. 138, 16–30. https://doi.org/10.1016/j.quascirev.2016.02.022.

Giraudi, C., 2015. The upper Pleistocene deglaciation on the Apennines (Peninsular Italy). Cuad. Investig. Geogr. 41, 87–105. https://doi.org/10.18172/cig.2696.

Gómez-Ortiz, A., Palacios, D., Palade, B., Vázquez-Selem, L., Salvador-Franch, F., 2012. The deglaciation of the Sierra Nevada (southern Spain). Geomorphology 159, 93–105. https://doi.org/10.1016/j.geomorph.2012.03.008.

González-Sampériz, P., Valero-Garcés, B.L., Moreno, A., Jalut, G., García-Ruiz, J.M., Martí-Bono, C., Delgado-Huertas, A., Navas, A., Otto, T., Dedoubat, J.J., 2006. Climate variability in the Spanish Pyrenees during the last 30,000 yr revealed by the El Portalet sequence. Quat. Res. 66 (1), 38–52. https://doi.org/10.1016/j.yqres.2006.02.004.

Guérin, G., Mercier, N., Adamiec, G., 2011. Dose-rate conversion factors: update. Anc. TL 29, 5–8.

Hambrey, M.J., Glasser, N.F., 2012. Discriminating glacier thermal and dynamic regimes in the sedimentary record. Sed. Geol. 251–252, 1–33. https://doi.org/10.1016/j.sedgeo.2012.01.008.

Hughes, P.D., Woodward, J.C., 2017. Quaternary glaciation in the Mediterranean mountains: a new synthesis. Geol. Soc. Lond. Spec. Publ. 433 (1), 1–23.

Ivy-Ochs, S., 2015. Glacier variations in the European Alps at the end of the last glaciation. Cuad. Investig. Geogr. 41, 45–65. https://doi.org/10.18172/cig.2750.

Ivy-Ochs, S., Kerschner, H., Maisch, M., Christl, M., Kubik, P.W., Schlüchter, C., 2009. Latest Pleistocene and Holocene glacier variations in the european Alps. Quat. Sci. Rev. 28 (21-22), 2137–2149. https://doi.org/10.1016/j.quascirev.2009.03.009.

Jalut, G., Dedoubat, J.J., Fontugne, M., Otto, T., 2009. Holocene circum-Mediterranean vegetation changes: climate forcing and human impact. Quat. Int. 200 (1-2), 4–18. https://doi.org/10.1016/j.quaint.2008.03.012.

Jiménez-Espejo, F.J., García-Alix, A., Jiménez-Moreno, G., Rodrigo-Gámiz, M., Anderson, R.S., Rodríguez-Tovar, F.J., Martínez-Ruiz, F., Giralt, S., Delgado Huertas, A., Pardo-Igúzquiza, E., 2014. Saharan aeolian input and effective humidity variations over western Europe during the Holocene from a high altitude record. Chem. Geol. 374–375, 1–12. https://doi.org/10.1016/j.chemgeo.2014.03.001.

Jiménez-Moreno, G., Anderson, R.S., 2012. Holocene vegetation and climate change recorded in alpine bog sediments from the Borreguiles de la Virgen, Sierra Nevada, southern Spain. Quat. Res. 77 (1), 44–53. https://doi.org/10.1016/j.yqres.2011.09.006.

Jiménez-Moreno, G., García-Alix, A., Hernández-Corbalán, M.D., Anderson, R.S., Delgado-Huertas, A., 2013. Vegetation, fire, climate and human disturbance history in the southwestern Mediterranean area during the late Holocene. Quat. Res. 79 (2), 110–122. https://doi.org/10.1016/j.yqres.2012.11.008.

Jiménez-Moreno, G., Rodríguez-Ramírez, A., Pérez-Asensio, J.N., Carrión, J.S., López-Sáez, J.A., Villarías-Robles, J.JR., Celestino-Pérez, S., Cerrillo-Cuenca, E., León, Á., Contreras, C., 2015. Impact of late-Holocene aridification trend, climate variability and geodynamic control on the environment from a coastal area in SW Spain. Holocene 25 (4), 607–617. https://doi.org/10.1177/0959683614565955.

Jiménez-Moreno, G., Anderson, R.S., Ramos-Román, M.J., Camuera, J., Mesa-Fernández, J.M., García-Alix, A., Jiménez-Espejo, F.J., Carrión, J.S., López-Avilés, A., 2020. The Holocene Cedrus pollen record from Sierra Nevada (S Spain), a proxy for climate change in N Africa. Quat. Sci. Rev. 242, 106468. https://doi.org/10.1016/j.quascirev.2020.106468.

Kuhlemann, J., Rohling, E.J., Krumrei, I., Kubik, P., Ivy-Ochs, S., Kucera, M., 2008. Regional synthesis of Mediterranean atmospheric circulation during the Last Glacial Maximum. Science 321 (5894), 1338–1340.

Knazková, M., Ňyvlt, D., Hrbáček, F., 2021. Slope processes connected with snow patches in semi-arid ice-free areas of James Ross Island, Antartic Peninsula. Geomorphology 373, 107479. https://doi.org/10.1016/j.geomorph.2020.107479.

Lagunas de Sierra Nevada, 2021. Laguna Seca. accessed 20 June 2021. https://lagunasdesierranevada.es/buscador-de-fotografias/entry/3381/.

Laskar, J., Robutel, P., Joutel, F., Gastineau, M., Correia, A.C.M., Levrard, B., 2004. A long-term numerical solution for the insolation quantities of the Earth. Astron. Astrophys. 428, 261–285. https://doi.org/10.1051/0004-6361:20041335.

Leontaritis, A.D., Kouli, K., Pavlopoulos, K., 2020. The glacial history of Greece: a comprehensive review. Med. Geosc. Rev. 2 (1), 65–90. https://doi.org/10.1007/s42990-020-00021-w.

López-Avilés, A., García-Alix, A., Jiménez-Moreno, G., Anderson, R.S., Toney, J.L., Mesa-Fernández, J.M., Jiménez-Espejo, F.J., 2021. Latest Holocene paleoenvironmental and paleoclimate reconstruction from an alpine bog in the Western Mediterranean region: The Borreguil de los Lavaderos de la Reina record (Sierra Nevada). Palaeogeogr. Palaeoclimatol. Palaeoecol. 573, 110434. https://doi.org/10.1016/j.palaeo.2021.110434.

Magny, M., 2001. Palaeohydrological changes as reflected by lake-level fluctuations in the Swiss Plateau, the Jura Mountains and the northern French Pre-Alps during the Last Glacial-Holocene transition: a regional synthesis. Glob. Planet. Change 30 (1-2), 85–101. https://doi.org/10.1016/S0921-8181(01)00080-7.

Magny, M., Aalbersberg, G., Bégeot, C., Benoit-Ruffaldi, P., Bossuet, G., Disnar, J.R., Heiri, O., Laggoun-Defarge, F., Mazier, F., Millet, L., Peyron, O., Vannière, B., Walter-Simonnet, A.V., 2006. Environmental and climatic changes in the Jura mountains (eastern France) during the Lateglacial-Holocene transition: a multi-proxy record from Lake Lautrey. Quat. Sci. Rev. 25, 414–445. https://doi.org/10.1016/j.quascirev.2005.02.005.

Magny, M., Peyron, O., Sadori, L., Ortu, E., Zanchetta, G., Vannière, B., Tinner, W., 2012. Contrasting patterns of precipitation seasonality during the Holocene in the south- and north-central Mediterranean. J. Quat. Sci. 27 (3), 290–296. https://doi.org/10.1002/jqs.1543.

Makos, M., 2015. Deglaciation of the high Tatra mountains. Cuad. Investig. Geogr. 41, 67–85. https://doi.org/10.18172/cig.2697.

Manzano, S., Carrión, J.S., López-Merino, L., Jiménez-Moreno, G., Toney, J.L., Amstrong, H., Anderson, R.S., García-Alix, A., Pérez, J.L.G., Sánchez-Mata, D., 2019. A palaeoecological approach to understanding the past and present of Sierra Nevada, a Southwestern European biodiversity hotspot. Glob. Planet. Change 175, 238–250. https://doi.org/10.1016/j.gloplacha.2019.02.006.

Martín Martín, J.M., Braga Alarcón, J.C., Gómez Pugnaire, M.T., 2010. Geological Routes of Sierra Nevada. Regional Ministry for the Environment, Junta de Andalucía.

Martrat, B., Jimenez-Amat, P., Zahn, R., Grimalt, J.O., 2014. Similarities and dissimilarities between the last two deglaciations and interglaciations in the North Atlantic region. Quat. Sci. Rev. 99, 122–134. https://doi.org/10.1016/j.quascirev.2014.06.016.

Mayya, Y.S., Morthekai, P., Murari, M.K., Singhvi, A.K., 2006. Towards quantifying beta microdosimetric effects in single-grain quartz dose distribution. Radiat. Meas. 41 (7-8), 1032–1039. https://doi.org/10.1016/j.radmeas.2006.08.004.

McCaroll, D., Knight, J., Rijsdijk, K., 2001. The glaciation of the Irish Sea Basin. J. Quat. Sci. 16, 391–506. https://doi.org/10.1002/jqs.640.

McDermott, F., 2004. Paleo-climate reconstruction from stable isotope variations in speleothems: a review. Quat. Sci. Rev. 23, 901–918. https://doi.org/10.1016/j.quascirev.2003.06.021.

Menzies, J., van der Meer, J.J.M., Rose, J., 2006. Till - as a glacial 'tectomict', its internal architecture, and the development of a 'typing' method for till differentiation. Geomorphology 75 (1-2), 172–200. https://doi.org/10.1016/j.geomorph.2004.02.017.

Mesa-Fernández, J.M., Jiménez-Moreno, G., Rodrigo-Gámiz, M., García-Alix, A., Jiménez-Espejo, F.J., Martínez-Ruiz, F., Scott Anderson, R., Camuera, J., Ramos-Román, M.J., 2018. Vegetation and geochemical responses to Holocene rapid climate change in the Sierra Nevada (southeastern Iberia): The Laguna Hondera record. Clim. Past 14, 1687–1706. https://doi.org/10.5194/cp-14-1687-2018.

Meyers, P.A., 1994. Preservation of elemental and isotopic source identification of sedimentary organic matter. Chem. Geol. 114 (3-4), 289–302. https://doi.org/10.1016/0009-2541(94)90059-0.

Meyers, P.A., 2003. Applications of organic geochemistry to paleolimnological reconstructions: a summary of examples from the Laurentian Great Lakes. Org. Geochem. 34 (2), 261–289. https://doi.org/10.1016/S0146-6380(02)00168-7.

Miall, A.D., 1978. Lithofacies types and vertical profile models in braided river deposits: a summary, in: Miall, A.D. (Eds.), Fluvial Sedimentology. Can. Soc. Petrol. Geol. 5, 597–604.

Mitchell, S.G., Humphries, E.E., 2015. Glacial cirques and the relationship between equilibrium line altitudes and mountain range height. Geology, 43, 35–38. https://doi.org/10.1130/G36180.1.

Morellón, M., Valero-Garcés, B., Vegas-Vilarrúbia, T., González-Sampériz, P., Romero, Ó., Delgado-Huertas, A., Mata, P., Moreno, A., Rico, M., Corella, J.P., 2009. Lateglacial and Holocene palaeohydrology in the western Mediterranean region: the lake estanya record (NE Spain). Quat. Sci. Rev. 28 (25-26), 2582–2599. https://doi.org/10.1016/j.quascirev.2009.05.014.

Moreno, A., González Sampériz, P., Morellón, M., Valero-Garcés, B.L., Fletcher, W.J., 2012. Northern Iberian abrupt climate change dynamics during the last glacial cycle: a view from lacustrine sediments. Quat. Sci. Rev. 36, 139–153. https://doi.org/10.1016/j.quascirev.2010.06.031.

Murray, A.S., Wintle, A.G., 2000. Luminescence dating of quartz using an improved single-aliquot regenerative-dose protocol. Radiat. Meas. 32 (1), 57–73. https://doi.org/10.1016/S1350-4487(99)00253-X.

Murray, A.S., Wintle, A.G., 2003. The single aliquot regenerative dose protocol: potential for improvements in reliability. Radiat. Meas. 37 (4-5), 377–381. https://doi.org/10.1016/S1350-4487(03)00053-2.

Nathan, R.P., Thomas, P.J., Jain, M., Murray, A.S., Rhodes, E.J., 2003. Environmental dose rate heterogeneity of beta radiation and its implications for luminescence

dating: Monte Carlo modelling and experimental validation. Radiat. Meas. 37 (4-5), 305–313. https://doi.org/10.1016/S1350-4487(03)00008-8.

Nemec, W., Steel, R.J., 1984. Alluvial and coastal conglomerates: their significant features and some comments on gravelly mass-flow deposits, in: Koster, E.H., Steel, R.J. (Eds.), Sedimentology of Gravels and Conglomerates. Can. Soc. Pet. Geol. 10, 1–31.

North Greenland Ice Core Project members., 2004. High resolution record of Northern Hemisphere climate extending into the last interglacial period. Nature, 431, 147–151. https://doi.org/10.1038/nature02805.

Oliva, M., Gómez-Ortiz, A., 2012. Late-Holocene environmental dynamics and climate variability in a Mediterranean high mountain environment (Sierra Nevada, Spain) inferred from lake sediments and historical sources. The Holocene 22 (8), 915–927. https://doi.org/10.1177/0959683611434235.

Oliva, M., Gómez-Ortiz, A., Palacios, D., Salvador-Franch, F., Salvà-Catarineu, M., 2014. Environmental evolution in Sierra Nevada (South Spain) since the last glaciation based on multi-proxy records. Quat. Int. 353, 195–209. https://doi.org/10.1016/j.quaint.2014.02.009.

Oliva, M., Gómez-Ortiz, A., Salvador-Franch, F., Salvà-Catarineu, M., Palacios, D., Tanarro, L., Ramos, M., Pereira, P., Ruiz-Fernández, J., 2016. Inexistence of permafrost at the top of the Veleta peak (Sierra Nevada, Spain). Sci. Total Environ. 550, 484–494. https://doi.org/10.1016/j.scitotenv.2016.01.150.

Organismo Autónomo Parques Nacionales (Ministerio para la Transición Ecológica y Reto Demográfico), 2021. Portal de descarga de datos meteorológicos. https://www.miteco.gob.es/es/red-parques-nacionales/red-seguimiento/acceso-datos.aspx (accessed 20 June 2021).

Palacios, D., Parilla, G., Zamorano, J.J., 1999. Paraglacial and postglacial debris flows on a Little Ice Age terminal moraine: Jamapa Glacier, Pico de Orizabo (México). Geomorphology, 28, 98-118. https://doi.org/10.1016/S0169-555X(98)00098-1.

Palacios, D., de Marcos, J., Vázquez-Selem, L., 2011. Last Glacial Maximum and Deglaciation of Sierra de Gredos, Central Iberian Peninsula. Quat. Int. 233 (1), 16–26. https://doi.org/10.1016/j.quaint.2010.04.029.

Palacios, D., Andrés, N., Marcos, J., Vázquez-Selem, L., 2012. Glacial landforms and their paleoclimatic significance in Sierra de Guadarrama, Central Iberian Peninsula. Geomorphology. 139–140, 67–78. https://doi.org/10.1016/j.geomorph.2011.10.003.

Palacios, D., de Andrés, N., López-Moreno, J.I., García-Ruiz, J.M., 2015a. Late Pleistocene deglaciation in the upper Gállego valley. Quat. Res. 83, 397–414. https://doi.org/10.1016/j.yqres.2015.01.010.

Palacios, D., Gómez-Ortiz, A., Andrés, N., Vázquez-Selem, L., Salvador-Franch, F., Oliva, M., 2015b. Maximum extent of late Pleistocene glaciers and last deglaciation of La Cerdanya mountains, southeastern Pyrenees. Geomorphology 231, 116–129. https://doi.org/10.1016/j.geomorph.2014.10.037.

Palacios, D., Gómez-Ortiz, A., Andrés, N., Salvador, F., Oliva, M., 2016. Timing and new geomorphologic evidence of the Last Deglaciation stages in Sierra Nevada (southern Spain). Quat. Sci. Rev. 150, 10–129. https://doi.org/10.1016/j.quascirev.2016.08.012.

Palacios, D., de Andrés, N., Gómez-Ortiz, A., García-Ruiz, J.M., 2017. Evidence of glacial activity during the Oldest Dryas in the mountains of Spain. Geol. Soc. Lond. Spec. Publ. 433 (1), 87–110. https://doi.org/10.1144/SP433.10.

Palacios, D., Oliva, M., Gómez-Ortiz, A., Andrés, N., Fernández-Fernández, J.M., Schimmelpfennig, I., Léanni, L., Team, A.S.T.E.R., 2020. Climate sensitivity and geomorphological response of cirque glaciers from the late glacial to the Holocene, Sierra Nevada. Spain. Quat. Sci. Rev. 248, 106617. https://doi.org/10.1016/j.quascirev.2020.106617.

Pallàs, R., Rodés, Á., Braucher, R., Carcaillet, J., Ortuño, M., Bordonau, J., Bourlès, D., Vilaplana, J.M., Masana, E., Santanach, P., 2006. Late Pleistocene and Holocene glaciation in the Pyrenees: a critical review and new evidence from ¹⁰Be exposure ages, south-central Pyrenees. Quat. Sci. Rev. 25 (21-22), 2937–2963. https://doi.org/10.1016/j.quascirev.2006.04.004.

Pallàs, R., Rodés, A., Braucher, R., Delmas, M., Calvet, M., Gunnell, Y., 2010. Small, isolated glacial catchments as priority targets for cosmogenic surface exposure dating of Pleistocene climate fluctuations, southeastern Pyrenees. Geology 38, 891–894. https://doi.org/10.1130/G31164.1.

Palma, P., Oliva, M., García-Hernández, C., Gómez Ortiz, A., Ruiz-Fernández, J., Salvador-Franch, F., Catarineu, M., 2017. Spatial characterization of glacial and periglacial landforms in the highlands of Sierra Nevada (Spain). Sci. Total Environ. 584–585, 1256–1267. https://doi.org/10.1016/j.scitotenv.2017.01.196.

Pedraza, J., Carrasco, R.M., Domínguez-Villar, D., Villa, J., 2013. Late Pleistocene glacial evolutionary stages in the gredos mountains (Iberian Central system). Quat. Int. 302, 88–100. https://doi.org/10.1016/j.quaint.2012.10.038.

Philippsen, B., 2013. The freshwater reservoir effect in radiocarbon dating. Herit. Sci. 1 (1), 24. https://doi.org/10.1186/2050-7445-1-24.

Powers, M.C., 1953. A new roundness scale for sedimentary particles. J. Sediment. Res. 23, 117–119. https://doi.org/10.1306/D4269567-2B26-11D7-8648000102C1865D.

Prescott, J.R., Hutton, J.T., 1994. Cosmic ray contributions to dose rates for luminescence and ESR dating: large depths and long-term variations. Radiat. Meas. 23, 497–500. https://doi.org/10.1016/1350-4487(94)90086-8.

Principato, S.M., Lee, J.F., 2014. GIS analysis of cirques on Vestfirðir, northwest Iceland: implications for palaeoclimate. Boreas 43 (4), 807–817. https://doi.org/10.1111/bor.12075.

Ramos-Román, M.J., Jiménez-Moreno, G., Anderson, R.S., García-Alix, A., Toney, J.L., Jiménez-Espejo, F.J., Carrión, J.S., 2016. Centennial-scale vegetation and North Atlantic Oscillation changes during the late Holocene in the western Mediterranean. Quat. Sci. Rev. 143, 84–95. https://doi.org/10.1016/j.quascirev.2016.05.007.

Ramos-Román, M.J., Jiménez-Moreno, G., Camuera, J., García-Alix, A., Anderson, R.S., Jiménez-Espejo, F.J., Sachse, D., Toney, J., Carrión, J.S., Webster, C., Yanes, Y., 2018a. Millennial-scale cyclical environment and climate variability during the Holocene in the western Mediterranean region deduced from a new multi-proxy analysis from the Padul record (Sierra Nevada, Spain). Glob. Planet. Change 168, 35–53. https://doi.org/10.1016/j.gloplacha.2018.06.003.

Ramos-Román, M.J., Jiménez-Moreno, G., Camuera, J., García-Alix, A., Anderson, R.S., Jiménez-Espejo, F.J., Carrión, J.S., 2018b. Holocene climate aridification trend and human impact interrupted by millennial- and centennial-scale climate fluctuations from a new sedimentary record from Padul (Sierra Nevada, southern Iberian Peninsula). Clim. Past 14 (1), 117–137. https://doi.org/10.5194/cp-14-117-2018.

Ramos-Román, M.J., Jiménez-Moreno, G., Anderson, R.S., García-Alix, A., Camuera, J., Mesa-Fernández, J.M., Manzano, S., 2019. Climate controlled historic olive tree occurrences and olive oil production in southern Spain. Glob. Planet. Change 182, 102996. https://doi.org/10.1016/j.gloplacha.2019.102996.

Reimer, P.J., Austin, W.E.N., Bard, E., Bayliss, A., Blackwell, P.G., Bronk Ramsey, C., Butzin, M., Cheng, H., Edwards, R.L., Friedrich, M., Grootes, P.M., Guilderson, T.P., Hajdas, I., Heaton, T.J., Hogg, A.G., Hughen, K.A., Kromer, B., Manning, S.W., Muscheler, R., Palmer, J.G., Pearson, C., van der Plicht, J., Reimer, R.W., Richards, D.A., Scott., E.M., Southon, J.R., Turney, C.S.M., Wacker, L., Adophi, F., Büntgen, U., Capano, M., Fahrni, S., Fogtmann-Schulz, A., Friedrich, R., Kudsk, S., Miyake, F., Olsen, J., Reinig, F., Sakamoto, M., Sookdeo, A., Talamo, S., 2020. The IntCal20 Northern Hemisphere radiocarbon calibration curve (0–55 cal kBP). Radiocarbon, 1–33. https://doi.org/10.1017/RDC.2020.41.

Ribolini, A., Bini, M., Isola, I., Spagnolo, M., Zanchetta, G., Pellitero, R., Mechernich, S., Gromig, R., Dunai, T., Wagner, B., Milevski, I., 2018. An oldest Dryas glacier expansion on Mount Pelister (Former Yugoslavian Republic of Macedonia) according to 10Be cosmogenic dating. J. Geol. Soc. Lond. 175 (1), 100–110. https://doi.org/10.1144/jgs2017-038.

Rodrigo-Gámiz, M., Martínez-Ruiz, F., Jiménez-Espejo, F.J., Gallego-Torres, D., Nieto-Moreno, V., Romero, O., Ariztegui, D., 2011. Impact of climate variability in the western Mediterranean during the last 20,000 years: oceanic and atmospheric responses. Quaternary Science Reviews 30 (15-16), 2018–2034. https://doi.org/10.1016/j.quascirev.2011.05.011.

Rolland, Y., Darnault, R., Braucher, R., Bourlès, D., Petit, C., Bouissou, S., 2020. Deglaciation history at the Alpine-Mediterranean transition (Argentera-Mercantour, SW Alps) from ¹⁰Be dating of moraines and glacially polished bedrock. Earth Surf. Process. Landf. 45 (2), 393–410. https://doi.org/10.1002/esp.4740.

Sancho, C., Peña-Monné, J.L., Lewis, C., McDonald, E., Rhodes, E., 2008. Actividad glaciar y desarrollo de terrazas durante el Pleistoceno Superior en Pirineos-Cuenca del Ebro. Geo-Temas 10, 763–766.

Sanders, J.W., Cuffey, K.M., MacGregor, K.R., Collins, B.D., 2013. The sediment budget of an alpine cirque. Bulletin 125 (1-2), 229–248. https://doi.org/10.1130/B30688.1.

Serrano, E., Gómez-Lende, M., Pellitero, R., González-Trueba, J.J., 2015. Deglaciation in the Cantabrian mountains: pattern and evolution. Cuad. Investig. Geogr. 41, 389–408. https://doi.org/10.18172/cig.2716.

Serrano, E., Oliva, M., González-García, M., López-Moreno, J.I., González-Trueba, J., Martín-Moreno, R., Gómez-Lende, M., Martín-Díaz, J., Nofre, J., Palma, P., 2018. Post-little ice age paraglacial processes and landforms in the high Iberian mountains: A review. Land. Degrad. Dev. 29 (11), 4186–4208. https://doi.org/10.1002/ldr.3171.

Simón, M., Sánchez, S., García, I., 2000. Soil-landscape evolution on a Mediterranean high mountain. Catena 39 (3), 211–231.

Sletten, K., Blikra, L.H., Ballantyne, C.K., Nesje, A., Dahl, S.O., 2003. Holocene debris flows recognized in a lacustrine sedimentary succession: sedimentology, chronostratigraphy and cause of triggering. Holocene 13 (6), 907–920. https://doi.org/10.1191/0959683603hl673rp.

Sohn, Y.K., Rhee, C.W., Kim, B.C., 1999. Debris flow and hyperconcentrated flood-flow deposits in an alluvial fan, Northwestern part of the Cretaceous Yongdong Basin, Central Korea. J. Geol. 107 (1), 111–132. https://doi.org/10.1086/314334.

Agencia Estatal de Meteorología, 2021. AEMet OpenData. http://www.aemet.es/es/datos_abiertos/AEMET_OpenData (accessed 20 June 2021).

Stuiver, M., Reimer, P.J., Reimer, R.W., 2021. CALIB 8.2 [WWW program]. http://calib.org/ (accessed 20 June 2021).

Toney, J.L., García-Alix, A., Jiménez-Moreno, G., Anderson, R.S., Moossen, H., Seki, O., 2020. New insights into Holocene hydrology and temperature from lipid biomarkers in western Mediterranean alpine wetlands. Quat. Sci. Rev. 240, 106395. https://doi.org/10.1016/j.quascirev.2020.106395.

Turu, V., Calvet, M., Bordonau, J., Gunnell, Y., Delmas, M., Vilaplana, J.M., Jalut, G., 2016. Did Pyrenean glaciers dance to the beat of global climatic events? Evidence for the Würmian sequence stratigraphy of an ice-dammed palaeolake depocentre in Andorra, in: Hughes, P.D., Woodward, J.C. (Eds.), Quaternary Glaciation in the Mediterranean Mountains. Geol. Soc. Lond., Spec. Publ. (On line). https://doi.org/10.1144/SP433.6.

Tyson, R.V., 1995. Sedimentary Organic Matter: Organic facies and palynofacies. Springer, Netherlands, Dordrecht, Netherlands. https://doi.org/10.1007/978-94-011-0739-6.

Valle, F., 2003. Mapa de series de vegetación de Andalucía, Ed. Rueda, Madrid.

Vonder-Haar, S.P., Hilton-Johnson, W., 1973. Mean magnetic susceptibility: A useful parameter for stratigraphic studies of glacial till. J. Sed. Petr. 43, 1148–1151. https://doi.org/10.1306/74D7292D-2B21-11D7-8648000102C1865D.

Zimmermann, M., Haeberli, W., 1992. Climatic change and debris flow activity in high-mountain areas. A case study in the Swiss Alps. Catena Suppl. 22, 59–72.